INVESTIGATION OF STRUCTUAL, FERROELECTRIC AND MAGNETIC PROPERTIES OF Gd DOPED BiFeO₃ NANOPARTICLES PREPARED BY SOL-GEL METHOD

A Dissertation Submitted to the Department of Physics, Bangladesh University of Engineering & Technology, Dhaka in Partial Fulfillment of Requirement for the Degree of Master of Science in Physics

SUBMITTED BY

MD. RAFIQ AZAD

EXAMINATION ROLL NO.: 1014142509F

SESSION: October 2014

DEPARTMENT OF PHYSICS

BANGLADESH UNIVERSITY OF ENGINEERING & TECHNOLOGY

DHAKA 1000, BANGLADESH

i

CANDIDATE'S DECLARATION

It is hereby declared that this thesis or any part of it has not been submitted elsewhere for the award of any degree or diploma.

Rasie
_____
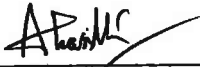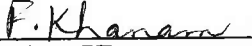
MD. RAFIQ AZAD

BANGLADESH UNIVERSITY OF ENGINEERING & TECHNOLOGY (BUET), DHAKA
DEPARTMENT OF PHYSICS

CERTIFICATION OF THESIS

The thesis titled **"INVESTIGATION OF STRUCTUAL, FERROELECTRIC AND MAGNETIC PROPERTIES OF Gd DOPED BiFeO₃ NANOPARTICLES PREPARED BY SOL-GEL METHOD"** submitted by **Md. Rafiq Azad,** Roll No-1014142509F, Registration No-1014142509F, Session: October-2014, has been accepted as satisfactory in partial fulfilment of the requirement for the degree of **Master of Science** (M. Sc.) in Physics on 25 April, 2016.

BOARD OF EXAMINERS

1. _____
   Dr. Mohammed Abdul Basith
   Associate Professor
   Department of Physics, BUET, Dhaka.

   Chairman
   (Supervisor)

2. _____
   Fahima Khanam
   Professor & Head
   Department of Physics, BUET, Dhaka.

   Member
   (Ex-Officio)

3. _____
   Dr. Md. Abu Hashan Bhuiyan
   Professor
   Department of Physics, BUET, Dhaka.

   Member

4. _____
   Dr. Muhammad Rakibul Islam
   Assistant Professor
   Department of Physics, BUET, Dhaka.

   Member

5. _____
   Dr. Abu Talib Md. Kaosar Jamil
   Professor
   Department of Physics
   Dhaka University of Engineering and Technology, Gazipur.

   Member
   (External)

DEDICATED

TO

MY BELOVED PARENTS

ACKNOWLEDGEMENTS

ABSTRACT

The nominal compositions of $BiFe_{1-x}Gd_xO_3$ (x = 0.00, 0.05) nanoparticles were synthesized using sol-gel method to investigate their structural, electrical, magnetic and optical properties. The investigated properties were compared between undoped and Gd-doped $BiFeO_3$ nanoparticles. The X-ray diffraction (XRD) patterns revealed that the substitution of Gd in the place of Fe in $BiFeO_3$ induces a tendency of phase transition from rhombohedral to orthorhombic. The field emission scanning electron microscopy images and their respective histograms demonstrated that due to the substitution of Gd, the average particle size was reduced with a narrow size distribution. Particularly, for 5 % Gd doped $BiFeO_3$ annealed at 600 ^{o}C the average particle size was reduced up to around ~35 nm which is much smaller than that of undoped $BiFeO_3$. From leakage current density vs. electric field graphs it was observed that the leaky behavior of the synthesized nanoparticles was suppressed due to Gd substitution and increasing annealing temperature. The suppression of leakage current density improved the ferroelectric behavior of the synthesized nanoparticles deduced from polarization vs. electric field hysteresis loops. The dielectric properties of the synthesized nanoparticles follow exactly the same trend of ferroelectric behavior and reduced leakage current density. The magnetization versus magnetic field hysteresis loops were carried out using a Superconducting Quantum Interface Device (SQUID) magnetometer at room temperature. The SQUID analysis demonstrated that, due to the Gd substitution in $BiFeO_3$ nanoparticles the room temperature magnetic parameters such as saturation magnetization (M_s) and remanent magnetization (M_r) decreased gradually with increasing annealing temperature, however, the values of M_s and M_r are many folds higher than their bulk counterparts. The magnetization parameters decreased may be due to the reduction of leakage current and oxygen vacancy related defects and also possibly some structural distortion due to Gd substitution. The band gap energy of the synthesized nanoparticles was determined which indicates that, it is possible to reduce band gap of multiferroic $BiFeO_3$ nanoparticles by doping Gd in the place of Fe.

Contents

Chapter 1
Introduction

Chapter 2
Theoretical Background

Chapter 3

Sample Preparation and Experimental Techniques

Chapter 4
Results and Discussion

Chapter 5
Summary and Conclusions

LIST OF FIGURES

LIST OF TABLE

Chapter 1

Introduction

1.1 Introduction

Multiferroic materials exhibit the coexistence of two or more of the primary ferro-orders such as (anti)ferroelectricity, (anti)ferromagnetism, and/or ferroelasticity in the same phase [1-5]. The combination of ferro-orders in multiferroics means that the different properties interact with each other. This then allows the possibility that one can switch magnetically ordered states using electric fields or vice versa i. e. electrically ordered states using magnetic fields [6]. These materials have attracted considerable research interest due to their potential in device miniaturization and high-density data storage system [7]. It is worth mentioning that multiferroic materials are the most promising materials for spintronic devices such as spin field effect transistors, electrical switching, nanoelectronics, magnetoelectric random access memories (MERAM), high frequency filters and sensors [8, 9]. Among compounds that are multiferroics, $BiFeO_3$ (BFO) is a paradigmatic and currently the most studied material, because it can exhibit multiferroic properties at room temperature [10]. The multiferroic $BiFeO_3$ is ferroelectric below $T_C \sim$ 1103 K and antiferromagnetic below $T_N \sim$ 643 K [11]. The $BiFeO_3$ have rhombohedrally distorted perovskite ABO_3 (A = Bi, B = Fe) structure with space group R3c and lattice parameters a = 5.58 Å and c = 13.87 Å [12-14]. For these properties BFO is one of the prime candidates for room temperature magnetoelectric applications [15]. BFO is found to exhibit weak ferromagnetic properties when the particle size is reduced down to nanoscale [16]. From literature reports it is apparent that the ferroelectric and magnetic properties of BFO could be due to the „A" site Bi ions and the „B" site Fe ions respectively [17]. In addition to this, any imbalance in the stoichiometric ratio between Bi, Fe and O ions also influences its multiferroic properties [18]. The investigation on the origin of magnetism in BFO could reveal interesting insights into their magnetic phenomena. BFO demonstrates enhanced magnetic properties through (i) the suppression of its cycloidal antiferromagnetic spin structures and (ii) the formation of

antiferromagnetic /ferromagnetic core/shell structures [13]. The magnetic property that occurs due to one of these origins would also influence other properties of BFO. On the other hand, BFO also exhibits visible light driven photocatalytic activities due to its smaller band gap, that currently being explored for applications such for hydrogen production via water splitting and degradation of organic pollutants [19, 20].

Previous investigations revealed that preparation of pure phase $BiFeO_3$ is a challenge [21-23] due to the formation of different impurity phases, such as $Bi_2Fe_4O_9$, $Bi_{36}Fe_{24}O_{57}$ and $Bi_{25}FeO_{40}$ [24, 25]. Bulk $BiFeO_3$ also exhibit by serious current leakage problems due to the existence of a large number of charge centers caused by oxygen ion vacancies [26]. These problems limit the use of $BiFeO_3$ for fabrication of multifunctional devices [6]. In order to reduce leakage current of BFO many attempts have been undertaken, for example: partial substitution of Bi^{3+}/Fe^{3+} by ions such as Sm^{3+}, Nd^{3+}, Gd^{3+}, Cr^{3+} etc. and preparation of nanoparticles [11]. Besides as was mentioned earlier $BiFeO_3$ have a spiral modulated spin structure (SMSS) with an incommensurate long-wavelength period of 62 nm [27]. This spiral spin structure cancels the macroscopic magnetization and prevents the observation of the linear magnetoelectric effect [28]. One of the easiest ways to destroy the SMSS in BFO is the structural modifications or deformations introduced by cation substitutions or doping [11]. Another way is the synthesis of the nanoparticles of $BiFeO_3$ with a particle size of the order of or smaller than 62 nm [6, 29].

The most widely used techniques for the synthesis of $BiFeO_3$ nanoparticles are based on different chemical routes such as sol-gel method, the electrospray method, the combustion synthesis process, sonochemical synthesis process etcetera [6, 29-31]. Therefore, in this investigation, we are interested to prepare Gd doped $BiFeO_3$ nanoparticles using the simple wet chemical technique, sol-gel to perturb the SMSS of BFO and to improve their ferroelectric and magnetic properties. Sol-gel method is chosen to prepare nanoparticles because this method involves molecular level mixing and results in homogeneous material [32]. This method also has an advantages over other chemical methods because of its low cost, generates less carbon residue and easy to prepare [33]. In this investigation, 5% Gd is substituted in the place of Fe in $BiFeO_3$ because so far there are a large number of reports on the doping effect of Gd^{3+} in place of Bi in $BiFeO_3$

nanoparticles [7, 20] but to the best of our knowledge no reports on the doping of Gd^{3+} in place of Fe in $BiFeO_3$ nanoparticles. Gd was chosen as a doping element because:

    i.   The effective magnetic moment of Gd^{3+} is large (8.0μB) [7] and the coupling between Gd^{3+} and Fe^{3+} can produce improved magnetism.

    ii. Gd^{3+} (0.938 Å) was used to substitute Fe^{3+} (0.645Å) because of its higher radius, which is expected to create more distortion in $BiFeO_3$ crystal structure and this distortion may enhance electrical polarization [34].

It is reported that $\geq$ 10% Gd doping in $BiFeO_3$ causes a structural transformation from rhombohedral to orthorhombic [7]. Therefore, here the Gd doping concentration was chosen as 5% so that crystal structure of the doped samples remain unchanged.

In this present investigation, nominal compositions of $BiFe_{1-x}Gd_xO_3$ (x = 0.00, 0.05) nanoparticles were synthesized by sol-gel method and their structure, particle size, magnetic, electrical, dielectric and optical properties were investigated. From these investigations it was observed that due to Gd substitution magnetic, electrical, dielectric and optical properties were improved at room temperature.

1.2 Aim and Objectives

The main objectives of the present research are as follows:

(a) Preparation of nanoparticles of $BiFe_{1-x}Gd_xO_3$ (x = 0.00, 0.05) multiferroic by using „Sol- gel" method.

(b) Investigation of the crystal structure of the synthesized nanoparticles using X-ray diffraction (XRD) techniques.

(c) Investigation of the particle size distribution of the synthesized nanoparticles using Field Emission Scanning Electron Microscopy (FESEM) imaging.

(d) Measurements of the magnetic properties such as saturation magnetization (M_s), remanent magnetization (M_r) and coercivity (H_c) of the synthesized nanoparticles from M-H curves obtained from Superconducting Quantum Interface Device (SQUID) magnetometer.

(e) Investigation of the ferroelectric properties of these multiferroic nanoparticles using a ferroelectric loop tracer (Polarization vs electric field).

(f) Investigation of the dielectric properties of the multiferroics as a function of frequency at room temperature.

(g) Investigation of the photocatalytic activity of the synthesized nanoparticles from optical measurements.

1.3 Outline of the Thesis

The thesis is organized as follows:

$\Rightarrow$ **Chapter 1** of this thesis deals with the introduction, importance of multiferroics and objectives of the present work.

$\Rightarrow$ **Chapter 2** gives a brief overview of the materials and theoretical background.

$\Rightarrow$ **Chapter 3** provides the details of the sample preparation and the description of different measurement techniques that have been used in this research work.

$\Rightarrow$ **Chapter 4** is dedicated to the results of various investigations of the study and explanation of results in the light of existing theories.

$\Rightarrow$ The conclusions drawn from the overall experimental results and discussion are presented in **Chapter 5.**

References:

[1] Eerenstein, W., Mathur, N. D., Scott, J. F., "Multiferroic and magnetoelectric materials", Nature, 442, 759, 2006.

[2] Cheong, S. W., Mostovoy, M., "Multiferroics: a magnetic twist for ferroelectricity", Nat. Mater., 6, 13, 2007.

[3] Ramesh, R., "Materials science: Emerging routes to multiferroics", Nature, 461, 1218, 2009.

[4] Wang, K. F., Liu, J. M., Z. F. Ren, Z. F., "Multiferroicity: the coupling between magnetic and polarization orders", Adv. Phys., 58, 321, 2009.

[5] Heron, J. T., Schlom, D. G., Ramesh, R., "Electric field control of magnetism using $BiFeO_3$-based heterostructures", Appl. Phys. Rev., 1, 021303, 2014.

[6] Basith, M. A., Ngo, D.-T., Quader, A., Rahman, M. A., Sinha, B. L., Bashir Ahmmad, Fumihiko Hirose and Molhave, K., "Simple top-down preparation of magnetic $Bi_{0.9}Gd_{0.1}Fe_{1-x}Ti_xO_3$ nanoparticles by ultrasonication of multiferroic bulk material", Nanoscale, 6, 14336, 2014.

[7] Lotey, G.S., Verma, N. K., "Structural, magnetic, and electrical properties of Gd-doped $BiFeO_3$ nanoparticles with reduced particle size", J. Nanopart Res., 14, 742, 2012.

[8] Kagawa, F., Horiuchi, S., Tokunaga, M., Fujioka, J., Tokura, Y., "Ferroelectricity in a one-dimensional organic quantum magnet", Nat. Phys., 6, 169, 2010.

[9] Wu, S. M., Cybart, S. A., Yu, P., Rossell, M. D., Zhang, J. X., Ramesh, R., Dynes, R. C., "Reversible electric control of exchange bias in a multiferroic field-effect device", Nat. Mater., 9, 756, 2010.

[10] Lazenka,V. V., Zhang, G., Vanacken, J., Makoed, I. I., Ravinski, A. F., Moshchalkov, V. V., "Structural transformation and magnetoelectric behaviour in $Bi_{1-x}Gd_xFeO_3$ multiferroics", J. Phys. D: Appl. Phys., 45, 125002, 2012.

[11] Basith, M. A., Kurni, O., Alam, M. S., Sinha, B. L. and Bashir Ahmmad, "Room temperature dielectric and magnetic properties of Gd and Ti co-doped $BiFeO_3$ ceramics", J. Appl. Phys., 115, 024102, 2014.

[12] Dutta, D. P., Mandal, B. P., Naik, R., Lawes, G., Tyagi, A. k., "Magnetic, Ferroelectric, and Magnetocapactive Properties of Sonochemically Synthesized Sc-Doped BiFeO$_3$ Nanoparticles", J. Phys. Chem., 117, 2382, 2013.

[13] Sarkar, M., Balakumar, S., Saravanan, P., Bharathkumar, S., "Compliments of Confinements: Substitution and Dimension Induced Magnetic Origin and Band-Bending Mediated Photocatalytic Enhancements in Bi$_{1-x}$Dy$_x$FeO$_3$ Particulate and Fiber Nanostructures", Nanoscale, 7, 10667, 2015.

[14] Madhu, C., Bellakki, M. B., Manivannan, V., "Synthesis and characterization of cation-doped BiFeO$_3$ materials for photocatalytic applications", In. J. Eng. Mater. S., 17, 131, 2010.

[15] Mukherjee, A., Basu, S., Manna, P. K., Yusuf, S. M., Pal, M., "Giant magnetodielectric and enhanced multiferroic properties of Sm doped bismuth ferrite nanoparticles", J. Phys. Chem. C., 2, 5885, 2014.

[16] Mazumder, R., Bhattacharya, P. S. D., Choudhury, P., Sen' A., Raja, M., "Ferromagnetism in nanoscale BiFeO$_3$", Appl. Phys. Lett., 91, 062510, 2007.

[17] Yang, C. H., Kan, D., Takeuchi, I., Nagarajan, V., Seidel, "Doping BiFeO$_3$: approaches and enhanced functionality", J., Phys. Chem. Chem. Phys., 14, 15953, 2012.

[18] Ederer, C., Spaldin, N. A., "Influence of strain and oxygen vacancies on the magnetoelectric properties of multiferroic bismuth ferrite", Phys. Rev. B., 71, 224103, 2005.

[19] Gao, F., Chen, X., Yin, K., Dong, S., Ren, Z., Yuan, F., Yu, T., Zou, Z., Liu, J. M., "Visible-Light Photocatalytic Properties of Weak Magnetic BiFeO$_3$ Nanoparticles", Adv. Mater., 19, 2889, 2007.

[20] Guo, R., Fang, L., Dong, W., Zheng, F., and Shen, M., "Enhanced Photocatalytic Activity and Ferromagnetism in Gd Doped BiFeO$_3$ Nanoparticles", J. Phys. Chem. C, 114, 21390, 2010.

[21] Ahmmad, B., Kanomata, K., Koike, K., Kubota, S., Kato, H., Hirose, F., Billah, Areef, Jalil, M. A., Basith, M. A., "Large difference between the magnetic properties of

Ba and Ti co-doped BiFeO$_3$ bulk materials and their corresponding nanoparticles prepared by ultrsonication", Under review, J. Phys. D: Appl. Phys.

[22] Jiang, Q.H., Nan, C.W., J. Am. Ceram., "Synthesis and Properties of Multiferroic La Modified BiFeO$_3$ Ceramics", J. Am. Ceram. Soc., 89, 2123, 2006.

[23] Ghosh, S., Dasgupta, S., Sen, A., Maiti, H. S., "Low-Temperature Synthesis of Bismuth Ferrite by Soft Chemical Route", J. Am. Cerm., Soc., 88, 1349, 2005.

[24] Munoz, T., Rivera, J. P., Monnier, A., Schmid, H., "Measurement of the Quadratic Magnetoelectric Effect on Single Crystalline BiFeO$_3$", Jpn. J. Appl. Phys., 24, 1051, 1985.

[25] Kumar, M., Yadav, K.L., "Study of room temperature magnetoelectric coupling in Ti substituted bismuth ferrite system", J. Appl. Phys., 100, 074111, 2006.

[26] Arya, G., Kumar, A., Ram, M., Negi, N. S., "Structural, Dielectric, Ferroelectric and Magnetic properties of Mn-doped BiFeO$_3$ nanoparticles synthesized by Sol-gel method", Int. J. Adv. Eng. Tech., 5, 245, 2013.

[27] Fischer, P., Polomska, M., Sosnowska, I., and Szymanski, M., "Temperature dependence of the crystal and magnetic structures of BiFeO$_3$", J. Phys. C: Solid State Phys., 13, 1931, 1980.

[28] Ederer, C., Spaldin, N. A., "Weak ferromagnetism and magnetoelectric coupling in bismuth ferrite", Phys. Rev. B., 71, 060401, 2005.

[29] Park, T. J., Papaefthymiou, G. C., Viescas, A. J., Moodenbaugh, A. R., Wong, S. S., "Size-Dependent Magnetic Properties of Single – Crystalline Multiferroic BiFeO$_3$ Nanoparticles", Nano Lett., 7, 766, 2007.

[30] Shirolkar, M. M., Hao, C., Dong, X., Guo, T., Zhang, L., Li, M., Wang, H., "Tunable Multiferroic and Bistable/Complementary Resistive Switching Properties of Dilutely Li–Doped BiFeO$_3$ Nanoparticles: An Effect of Aliovalent Substitution", Nanoscale, 6, 4735, 2014.

[31] Quinonez, J. L. O., Diaz, D., Dube, I. Z., Santamaria, H. A., Betancourt, I., Jacinto, P. S. and Etzana, N. N., "Easy Synthesis of High-Purity $BiFeO_3$ Nanoparticles: New Insights Derived from the Structural, Optical, and Magnetic Characterization", Inorg. Chem., 52, 10306, 2013.

[32] Verma, K., Sharma, S., Sharma, D. K., Kumar, R., Rai, R., "Sol-gel processing and characterization of nanometersized $(Ba,Sr)TiO_3$ ceramics", Adv. Mat. Lett., 3, 44, 2012.

[33] Suresh, P., Srinath, S., "A comparative study of sol-gel and solid-state prepared La^{3+} doped multiferroic $BiFeO_3$", Adv. Mat. Lett., 5, 127, 2014.

[34] Das, R.., Sarkar, T., Mandal, K., "Multiferroic properties of Ba^{2+} and Gd^{3+} co-doped bismuth ferrite: magnetic, ferroelectric and impedance spectroscopic analysis", J. Phys. D: Appl. Phys., 45, 455002, 2012.

Chapter 2

Theoretical Background

2.1 Introduction:

Electricity and magnetism were combined into one common discipline in the 19th century, culminating in the Maxwell equations [1]. These equations tell us about the unified nature of magnetism and electricity. But electric and magnetic ordering in solids are most often considered separately and usually with good reason: the electric charges of electrons and ions are responsible for the charge effects, whereas electron spins govern magnetic properties. There are, however, cases where these degrees of freedom couple strongly. For example, in the new, large field of spintronics, the effects of spins on the transport properties of solids (and vice versa) allow the possibility to control one by the other. The finding of a strong coupling of magnetic and electric degrees of freedom in insulators can be traced back to Pierre Curie, but the real beginning of this field started in 1959 with a short remark by Landau and Lifshitz in a volume of their Course of Theoretical Physics [2].

2.2 Multiferroics

The term multiferroic was first used by H. Schmid in 1994 [3]. Multiferroics are single phase materials which simultaneously possess two or more primary ferroic order parameter. The four basic primary ferroic order parameters are:

- ferromagnetism
- ferroelectricity
- ferroelasticity
- ferrotoroidicity

The definition of multiferroics can be expanded to include non-primary order parameters, such as antiferromagnetism, ferrimagnetism and antiferroelectricity.
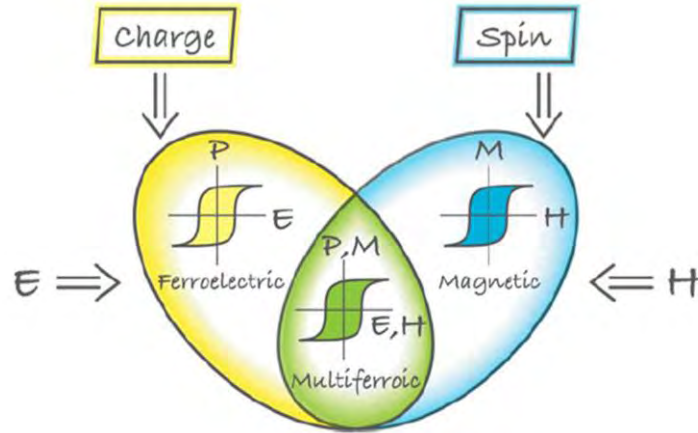
Figure 2.1: A schematic diagram of multiferroic

If the coupling between electric and magnetic order parameters exists, a multiferroic material becomes a magnetoelectric material. But a magnetoelectric (or a multiferroic) material does not necessary to be a multiferroic (or a magnetoelectric) material [4]. The history of magnetoelectric multiferroics can be traced back to the 1960s [5]. In the most general sense the field of multiferroics was born from studies of magnetoelectric systems. In recent 10 years, there is a great revival in multiferroics. In 2000, Nicola A. Hill gave an answer about scarcity of ferromagnetic ferroelectric coexistence [6]. In 2003 the large ferroelectric polarization was discovered in epitaxially grown thin films of $BiFeO_3$ [7]. The same year, the strong magnetic and electric coupling was found in orthorhombic $TbMnO_3$ [8] and $TbMn_2O_5$ [9]. The recent studies of multiferroics show the importance of collaboration between experiment technology and modeling design.

2.2.1 Classification of multiferroics

Multiferroic materials can broadly be classified in two categories namely single phase and composite materials. Single phase multiferroic materials show both ferroelectric and ferromagnetic order and they have similar crystal structure [10-16]. For the case of single phase multiferroic, multiferroicity is intrinsic effect of the material.

Composite multiferroic materials results from the combination of two materials, those are ferroelectric and ferromagnetic separately. For the case of composite multiferroic,

multiferroic order is not intrinsic and they have different structures. The scarcity of single phase multiferroic materials makes composite materials alternative [17-23].

Single phase multiferroics can be classified into two big groups according to Khomskii classification [24].

a) Type-I multiferroics
b) Type-II multiferroics

Type-I multiferroics

Type-I multiferroics are those materials in which ferroelectricity and magnetism have different sources; usually they show large polarization values and ferroelectricity appears at much higher temperatures than magnetism. This difference in transition temperatures reveals that both orders involve different energy scales and mechanisms, which provokes the occurrence of weak magnetoelectric coupling. $BiFeO_3$ is the example of type-1 multiferroic.

Type-II multiferroics

Type-II multiferroic is novel class of multiferroics in which ferroelectricity exists only in a magnetically ordered state and caused by a particular type of magnetism. Type-II multiferroics divided into two groups: those in which ferroelectricity is caused by a particular type of magnetic spiral and those in which ferroelectricity appears even for collinear magnetic structures. $TbMnO_3$ is the example of type-II multiferroic.

2.3 Ferroelectric Materials:

Ferroelectricity is a property of certain materials that have a spontaneous electric polarization that can be reversed by the application of an external electric field. The electrical analogue of the phenomenon of ferromagnetism was discovered in 1920 [25], when it was found that crystals of Rochelle salt (sodium potassium tartrate tetra hydrate) possess spontaneous polarization, the direction of which can be reversed by the

application of a strong enough electric field. This property was called 'ferroelectricity', by analogy with ferromagnetism (even though no iron or spontaneous magnetization is present in the crystal).

A more familiar, and simpler, example of a ferroelectric crystal is barium titanate, $BaTiO_3$.
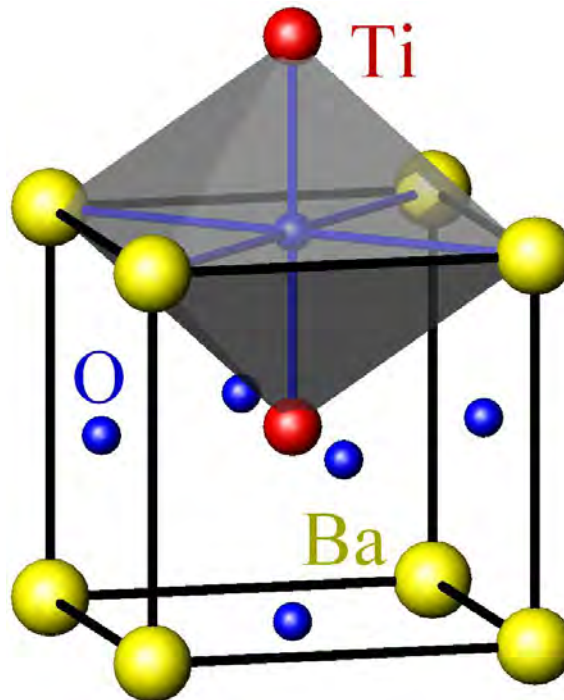
Figure 2.2: Barium titanate ($BaTiO_3$).

Above 130 °C it has a crystal structure such that a macroscopic polarization (i.e. electric dipole moment per unit volume) can arise in it only when an electric field is applied. This is a 'paraelectric' phase, and the polarization is a single-valued function of the applied electric field. The directional symmetry of this phase is the same as that of a cube. On cooling below 130 °C there is a phase transition to a crystal structure in which the centroids of the positive charges and the negative charges do not coincide, so there is a net dipole moment or polarization, even when no external electric field is present. This spontaneous polarization can point along any of six equivalent directions (parallel or antiparallel to any edge of the cube which is the repeat unit for the crystal structure of the paraelectric phase or the parent phase), giving rise to the possibility of six ferroelectric

domain types. So we once again get hysteresis when we plot the net macroscopic polarization of a specimen crystal as a function of increasing and decreasing electric field. The six orientation states or domain states are equally stable. This means that if a part of the ferroelectric crystal is in a particular orientation state, there is no reason why it should, on its own free volition, want to switch to another domain state.

One of the very active areas of current research is to exploit this property for storage of information in computer memories and other memories. Thin films, rather than bulk single crystals, of ferroelectrics are more suitable for this application. And compared to barium titanate, some of the more suitable ferroelectrics are barium strontium titanate (BST), lead zirconate titanate (PZT), and lanthanum-doped bismuth titanate (BLT). The 'up' and 'down' states of the spontaneous polarization in a ferroelectric domain provide the basis for the 0 (1 binary logic used in the memory device. And since the 0 and 1 states are equally stable, there is no need to apply a biasing electric field to make a memory-configuration 'nonvolatile'. This is particularly useful for applications in smart cards. NVFRAMs (nonvolatile ferroelectric random-access memories) may eventually replace many of the existing memories in computer applications.

Another likely application of ferroelectric thin films in computers is for making DRAMS (dynamic random-access memories) [26]. These will exploit another important aspect of ferroelectric materials, namely a usually high dielectric permittivity in the vicinity of the ferroelectric phase transition. High permittivity is preferred for making capacitors, because it enables us to reduce the size of the capacitor.

The internal electric dipoles of a ferroelectric material are coupled to the material lattice so anything that changes the lattice will change the strength of the dipoles (in other words, a change in the spontaneous polarization). The change in the spontaneous polarization results in a change in the surface charge. This can cause current flow in the case of a ferroelectric capacitor even without the presence of an external voltage across the capacitor. Two stimuli that will change the lattice dimensions of a material are force and temperature. The generation of a surface charge in response to the application of an external stress to a material is called piezoelectricity. A change in the spontaneous polarization of a material in response to a change in temperature is called pyroelectricity.

2.4 Magnetic behavior

The phenomenon of magnetism has been known to mankind for many thousands of years. Lodestone (Fe_3O_4) was the first permanent magnetic material to be identified and studied. The magnetic moment of an atom/ion has three principal sources:

a) The spin of electrons

b) Electron orbital angular momentum about the nucleus and

c) A change in the orbital moment induced by an applied magnetic field.

The first two effects give paramagnetic contributions to the magnetization and the third gives a diamagnetic contribution [27].

In a crystal, the magnetic property depends on two factors: (i) the magnetic moment associated with each atom/ion, and (ii) the interactions between these magnetic moments. In the case that there are no unpaired electrons around each atom/ion, there will be no net magnetic moments.

The magnetic behavior of materials can be classified into the following five major groups:

i. Diamagnetism

ii. Paramagnetism

iii. Ferromagnetism

iv. Antiferromagnetism

v. Ferrimagnetism

i. Diamagnetism

The substances whose atoms have zero resultant magnetic moment are called as diamagnetic substances. The behavior of diamagnetic substances in external magnetic field is known as diamagnetism, a fundamental property of all matter. In the absence of external magnetic field atoms of diamagnetic substances have zero resultant magnetic moment. If the diamagnetic substance is placed in external magnetic field then magnetic lines of induction will pass through electronic orbits. This will produce induced current. The induced current produces induced magnetic moment in opposite direction to that of the applied field. Hence atomic magnets of diamagnetic substances will align in opposite

direction to that of the direction of external magnetic field. The resultant magnetic moment of the substance increases and it will show weak magnetic property. The diamagnetic substances are slightly repelled by the magnet. In diamagnetic materials the magnetic susceptibility is negative. Usually its magnitude is of the order of -10^{-6} to -10^{-5}. Diamagnetic materials have a relative magnetic permeability that is less than 1. In diamagnetic materials the susceptibility nearly has a constant value independent of temperature. Most of the materials are diamagnetic e.g. Mercury, air, water, alcohol, gold, bismuth, copper, hydrogen, zinc, diamond, NaCl, nitrogen, magnesium, silver etc.

ii. Paramagnetism

The substances whose atoms have resultant magnetic dipole moment slightly greater than zero are called as paramagnetic substances. The behaviour of paramagnetic substances in external magnetic field is known as paramagnetism. In the absence of external magnetic field atomic magnets of paramagnetic substances will point out in all possible directions (Figure 2.3a). Hence the resultant magnetic moment of the substance will be less and it will not show magnetic property. If the paramagnetic substance is placed in a magnetic field then atomic magnets of paramagnetic substances will align in the same direction as that of the direction of external magnetic field. Hence resultant magnetic moment of the substance increases and it will show magnetic property. Paramagnetic materials attract and repel like normal magnets when subjected to a magnetic field. Under relatively low magnetic field saturation when the majority of the atomic dipoles are not aligned with the field, paramagnetic materials exhibit magnetization. In paramagnetic material alignment of the atomic dipoles with the magnetic field tends to strengthen it, and is described by a relative magnetic permeability, μ_r greater than unity (or, equivalently, a small positive magnetic susceptibility greater than zero). The susceptibility is however is also very small with the order of 10^{-4} to 10^{-5}.

A few examples of paramagnetic materials are oxygen, glass, paper, aluminium, platinum, chromium, sodium, manganese, copper chloride etc. The susceptibility of a paramagnetic material is inversely dependent on temperature and related with Curie law [28]

$$\chi = \frac{C}{T} \tag{2.1}$$

Where C is the Curie constant.
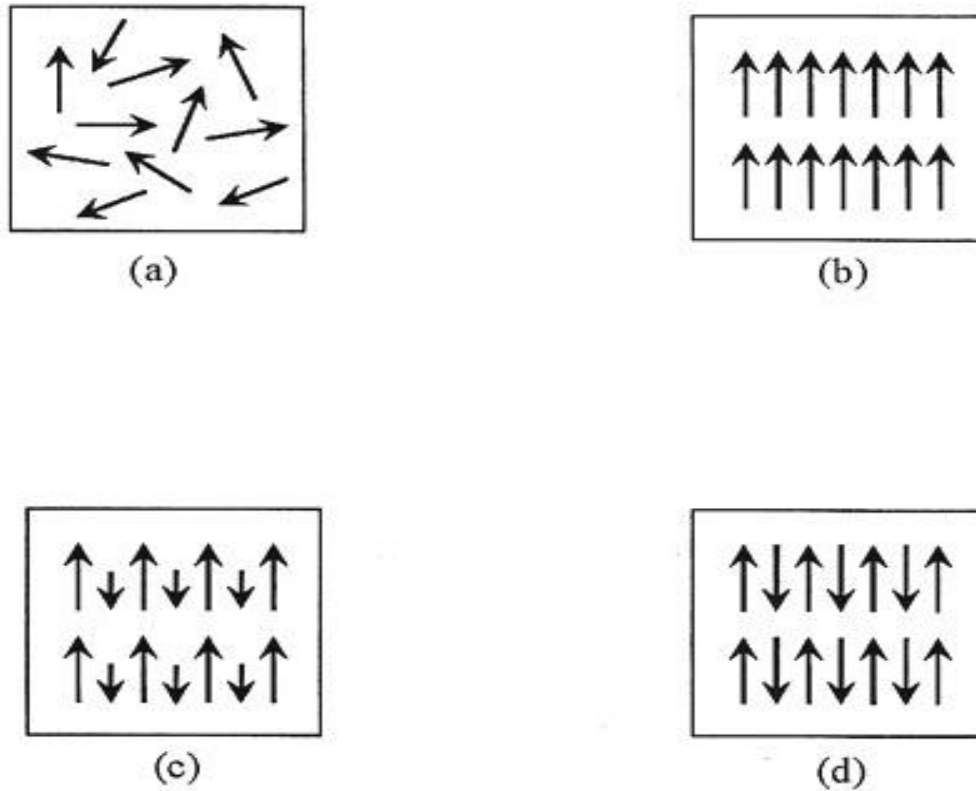
Figure 2.3: Varieties of magnetic orderings (a) paramagnetic, (b) ferromagnetic, (c) ferromagnetic and (d) antiferromagnetic.

iii. Ferromagnetism

The substances whose atoms have resultant magnetic dipole moment greater than diamagnetic and paramagnetic substances are called as ferromagnetic substances. The behavior of ferromagnetic substances in external magnetic field is known as ferromagnetism. In the absence of external magnetic field atomic magnets of ferromagnetic substance interact with each other and forms the groups called as domains.

In the absence of external magnetic field, domains of the ferromagnetic substances will point out in all possible direction. Hence resultant magnetic moment of the substance will be less and it will not show magnetic property. If the ferromagnetic substance is placed in a weak magnetic field then, some domains will point out in same direction as that of external magnetic field (Figure 2.3b). Hence the resultant magnetic moment of the substance increases and it will show magnetic property. If external magnetic field is removed from the substance then domains of substances will point out in all possible direction. Hence the resultant magnetic moment of the substance decreases to its original value and it loses magnetic property. If the ferromagnetic substance is placed in a strong magnetic field then, all domains of substance will align in the same direction as that of the direction of external magnetic field. In this case, domains will grow in their size also. Hence resultant magnetic moment of substance increases largely and it will show strong magnetic property. If the external magnetic field is removed from the substance then domains of the substance will remain in the same direction. Hence resultant magnetic moment of the substance remains to its maximum value. Therefore, it will not lose magnetic property. The permeability of ferromagnetic substance is much greater than 1. Some well-known ferromagnetic materials are: Ni, Co, Fe, Gd and many of their alloys. The susceptibility of ferromagnetic material does not follow the Curie law, but displayed a modified behavior defined by Curie-Weiss law [29]

$$\chi = \frac{C}{T - \theta}$$ (2.2)

Where C is a constant and θ is called Weiss constant. For ferromagnetic materials, the Weiss constant is almost identical to the Curie temperature (T_c).

The two distinct characteristics of ferromagnetic materials are:

➢ Spontaneous magnetization and

➢ The existence of magnetic ordering temperature.

The spontaneous magnetization is the net magnetization that exists inside a uniformly magnetized microscopic volume in the absence of a field. The magnitude of this magnetization, at 0 K, is dependent on the spin magnetic moments of electrons. The saturation magnetization is the maximum induced magnetic moment that can be obtained in a magnetic field; beyond this field no further increase in magnetization occurs.

Saturation magnetization is an intrinsic property, independent of particle size but dependent on temperature.

iv. Antiferromagnetism

Materials that are antiferromagnetic are similar to ferromagnetic materials. However, in an antiferromagnetism the dipoles have equal moments and adjacent dipoles point in opposite directions (Figure 2.3d). Thus the moments balance each other, resulting in a zero net magnetization. Antiferromagnetism are mostly observed at low temperature. In varying temperature, antiferromagnets can be seen to exhibit diamagnetic and ferromagnetic properties. The antiferromagnetic susceptibility is followed by the Curie-Weiss law with a negative θ as in equation 2.2.

Common examples of materials with antiferromagnetic ordering are MnO, FeO, CoO and NiO [30].

v. Ferrimagnetism

Ferrimagnetism is a special case of antiferromagnetism, where the material consists of a lattice of rigidly alternating spins of different magnitudes (Figure 2.3c). As in antiferromagnetism, the adjacent magnetic spins align antiparallel. However, since the adjacent spins are of different magnitudes, the resulting material exhibits a net magnetic moment in the absence of an applied magnetic field. The behavior of susceptibility of a ferrimagnetic material also obeys Curie-Weiss law and has a relative permeability greater than 1. In ionic compounds, such as oxides, more complex forms of magnetic ordering can occur as a result of the crystal structure. In ferromagnetic material the magnetic structure is composed of two magnetic sublattices (called A and B) separated by oxygens. The exchange interactions are mediated by the oxygen anions. When this happens, the interactions are called indirect or superexchange interactions. The strongest superexchange interactions result in an antiparallel alignment of spins between the A and B sublattice. In ferrimagnets, the magnetic moments of the A and B sublattices are not equal and result in a net magnetic moment. Ferrimagnetism is therefore similar to ferromagnetism. It exhibits all the hallmarks of ferromagnetic behavior spontaneous

magnetization, Curie temperatures, hysteresis, and remanence. However, ferro- and ferrimagnets have very different magnetic ordering.

2.5 Hysteresis Loop

In addition to the Curie temperature and saturation magnetization, ferromagnets and ferrimagnets can retain a memory of an applied field once it is removed. This behavior is called hysteresis and a plot of the variation of magnetization with magnetic field is called a hysteresis loop (Figure 2.4).
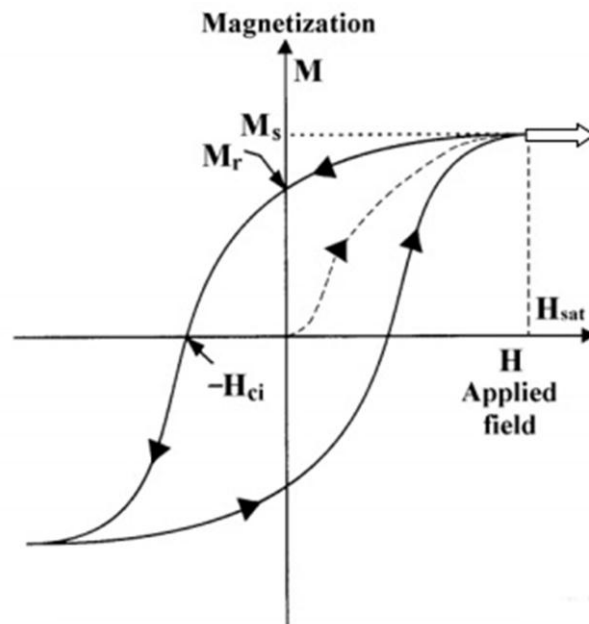
Figure 2.4: Hysteresis loop for a ferromagnetic material

The performance of any magnetic material can be defined with the help of this hysteresis loop. M_s is the saturation magnetization and is a measure of how strongly the material can be magnetized. M_r is the remanent magnetization which is the residual, permanent magnetization left after the removal of the applied field. In order to demagnetize the specimen from its remanent state, a reverse field H_{ci}, the coercive field is required to reduce the residual magnetization to zero. Depending on the value of the coercive field, ferromagnetic materials are classified as hard or soft. A hard magnet needs a large field to reduce its residual magnetization to zero, and for a soft magnet a small field is required to reduce its residual magnetization to zero. Hard and soft magnetic materials obviously

have totally complementary applications. The various hysteresis parameters are not solely intrinsic properties but are dependent on grain size, domain state, stresses, and temperature.

2.6 Ferroelastic material

Ferroelasticity is a phenomenon in which a material may exhibit a spontaneous strain. In ferroics, ferroelasticity is the mechanical equivalent of ferroelectricity and ferromagnetism. When stress is applied to a ferroelastic material, a phase change will occur in the material from one phase to an equally stable phase, either of different crystal structure (e.g. cubic to tetragonal), or of different orientation (a 'twin' phase). This stress-induced phase change results in a spontaneous strain in the material.

A crystal is ferroelastic if it has two or more stable orientational states in the absence of mechanical stress or electric field, and if it can be reproducibly transformed from one to another of these states by the application of mechanical stress [31]. Ferroelasticity is a structure-dependent property and is directly inferable from the crystal structure. The onset of ferroelasticity, as a function of temperature or pressure, is often accompanied by additional cooperative phenomena. When stresses are applied to a ferroelastic material, one observes a highly non-Hookian strain- stress curve termed a hysteresis [32]. The largest class of materials with ferroic properties comprises ferroelastics, with a significant number of applications such as piezoelectric sensors and mechanical switches. Many ferroelectric and ferromagnetic device materials are also ferroelastic such that multiferroicity plays a large role in ferroelastic materials. Nevertheless, the desired device properties are related mainly to ferroelectric and ferromagnetic switching. Thus, one may think that ferroelasticity plays only a minor role in the search for multiferroic materials. This is not the case, however. Strain and ferroelasticity seem to mediate much of the coupling between ferroelectric and ferromagnetic properties. So a good understanding of ferroelastic properties is central to much wider research on the switching behavior of ferroelectric, ferromagnetic, and multiferroic materials. Ferroelasticity is defined by its hysteresis, as are its sister ferroic properties, ferroelectricity and ferromagnetism. An elastic hysteresis represents the effect of the mechanical switching between at least two orientation states of a crystal by external

stress. One of the first full hysteresis loops was seen in 1976 for the prototypic material $Pb_3(PO_4)_2$ [33].
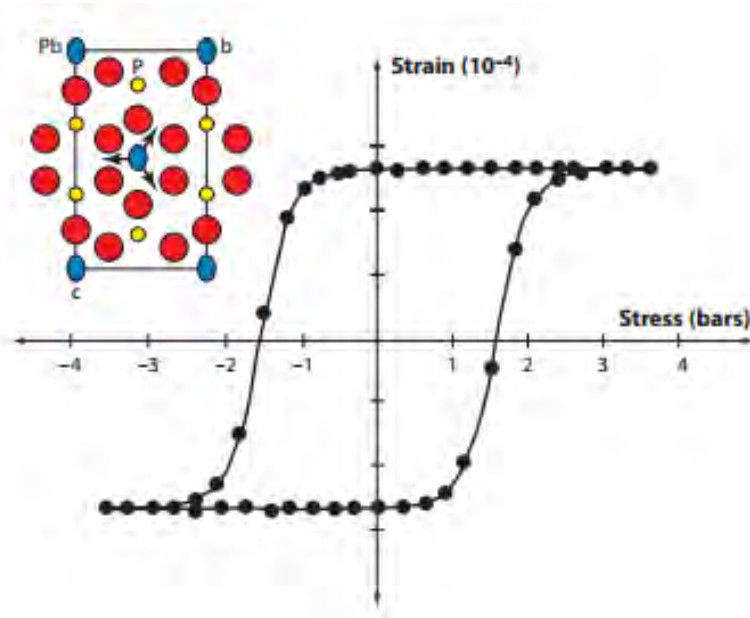
Figure 2.5: Ferroelastic hysteresis and atomic switching in $Pb_3(PO_4)_2$

The structural mechanism for ferroelasticity originates from the shift of the Pb atom away from the center of its oxygen cage towards one pair of oxygen. This leads to a monoclinic distortion of the crystal structure that can be inverted or rotated (in the direction of the arrows in figure 2.5) under external stress.

The size of the ferroelastic hysteresis depends on thermodynamic parameters such as temperature T, pressure P, or chemical composition N. Most ferroelastic materials show phase transitions between a ferroelastic phase and a paraelastic phase. The essential parameter is then the spontaneous strain, i.e., the deformation of the crystal generated by the phase transition, which has to have at least two orientations between which switching may occur. Mobile domain boundaries in magnetism play a major role in the construction of memory devices. Their speed and nucleation under applied magnetic fields are very well understood and are reproducible in an engineering manner [34]. Such boundaries form the base for spintronics [35].

2.7 Ferrotoroidal Material

Ferroic phenomenon or the presence of switchable domain walls in an external field is a direct consequence of a specific broken symmetry [36]. Loss of spatial inversion symmetry results in ferroelectricity whereas loss of time reversal symmetry results in ferromagnetism. Ferroelasticity is a result of broken rotational symmetry although it remains invariant under both spatial inversion and time reversal symmetries. The fourth possibility corresponds to when both spatial inversion and time reversal symmetries are simultaneously broken. This is the case for recently discovered ferrotoroidic materials [37] where the long-range order is related to an ordering of magnetic vortex-like structures characterized by a toroidal dipolar moment. It is important to mention that the ferrotoroidic order is also related to magnetoelectric behavior [38] which is one of the main attractions of multiferroics–materials that exhibit two or more ferroic orders simultaneously.

A phase transition to spontaneous long-range order of microscopic magnetic toroidal moments has been termed "ferrotoroidicity". It is expected to fill the symmetry schemes of primary ferroics (phase transitions with spontaneous point symmetry breaking) with a space-odd, time-odd macroscopic order parameter. A ferrotoroidic material would exhibit domains which could be switched by an appropriate field, e.g. a magnetic field curl.

The existence of ferrotoroidicity is still under debate and clear-cut evidence has not been presented yet mostly due to the difficulty to distinguish ferrotoroidicity from antiferromagnetic order, as both have no net magnetization and the order parameter symmetry is the same.

2.8 Dielectrics

A dielectric material is an electrical insulator that can be polarized by an applied electric field as shown in figure 2.6. The word dielectric is derived from the prefix dia, originally from Greek, which means „through" or „across", thus the dielectric is referred to as a material that permits the passage of the electric flux but not particles. When a dielectric is placed in an electric field, electric charges do not flow through the materials as in a conductor, but only slightly shift from their average equilibrium positions causing dielectric polarization. Because of dielectric polarization, positive charges are displaced towards the field and negative charges shift in the opposite direction. This creates an internal electric field which reduces the overall field within the dielectric itself. If a dielectric is composed of weakly bonded molecules, those molecules not only become polarized, but also reorient so that their symmetry axes align to the field.
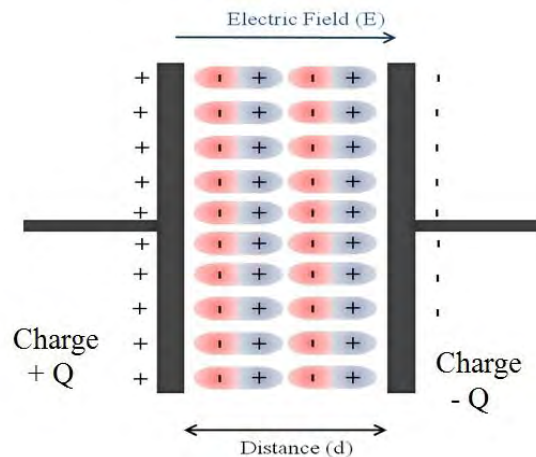
Figure 2.6: Schematic diagram of parallel electrodes separated by a dielectric material

There are two types of dielectric; they are polar dielectrics and non-polar dielectrics. In polar dielectric, a shift has occurred in the atomic structures such that the positive and negative charges have an asymmetrical alignment producing an electrical dipole but in non-polar dielectric this situation is absent.

2.8.1 Dielectric Polarization

When the atoms or molecules of a dielectric are placed in an external electric field, the nuclei are pushed with the field resulting in an increased positive charge on one side while the electron clouds are pulled against it resulting in an increased negative charge on the other side. This process is known as polarization and a dielectric material in such a state is said to be polarized [39]. There are two principal methods by which a dielectric can be polarized, stretching and rotation.

2.8.2 Process of Polarization

The formation of an electric dipole or polarization can happen in a number of process or mechanisms. At different frequency regimes each one contributes to dielectric response and their involvement are in different polarizable species. The basic mechanism or processes which occur polarization in dielectrics are:

1)   Electronic polarization

2)   Ionic or atomic polarization

3)   Orientation or dipolar polarization

4)   Interfacial or space charge polarization

2.8.2.1 Electronic Polarization

Electronic polarization occurs in all dielectric materials. Upon an external electric field being applied a slight relative shift of positive and negative electric charge in opposite directions occurs within an insulator, or dielectric. Polarization occurs when the induced electric field distorts the negative cloud of electrons around positive atomic nuclei in a direction opposite the field. This slight separation of charge makes one side of the atom somewhat positive and the opposite side somewhat negative. As soon as the electric field is removed the electrons and nuclei return to their original position and the polarization disappears. Electronic polarization is independent of temperature. Mono-atomic gases exhibit only electronic polarization.

No Field   **Field Applied**

E

Electronic Polarization
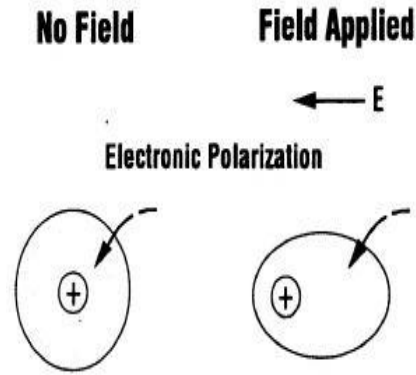
Figure 2.7: Electronic polarization

2.8.2.2   Ionic or atomic polarization

Atomic polarization is observed when the nucleus of the atom reorients in response to the electric field. This is a resonant process. Atomic polarization is intrinsic to the nature of the atom and is a consequence of an applied field. Electronic polarization refers to the electron density and is a consequence of an applied field. Atomic polarization is usually small compared to electronic polarization.

Various popular effects like piezoelectricity, pyroelectricity, ferroelectricity etc occurs by ionic polarization phenomena. Wide range of polarization effects are possible through this mechanism depending upon the crystal structure, solid solution and various other factors. Ionic polarization is inversely proportional to the mass of the ions and square of the natural frequency of vibration of the ions. Covalently bonded ceramics do not show ionic polarization due to lack of charged atoms, but ionic bonded structures (for example: NaCl, KCl and LiBr) shows ionic polarization.

No Applied Field

With Applied Field
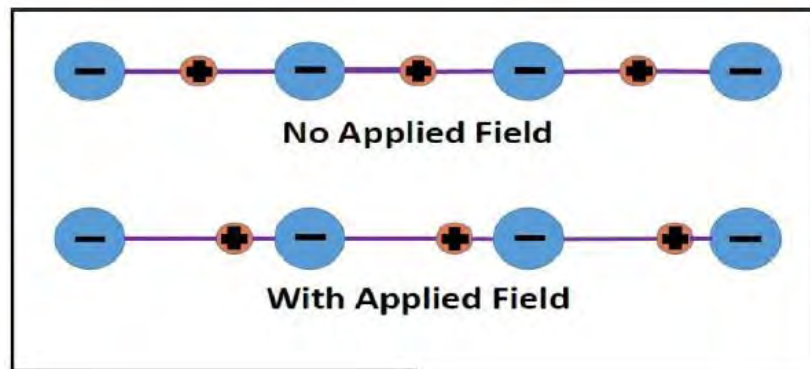
Figure 2.8: Ionic or atomic polarization

2.8.2.3 Orientation or dipolar polarization

Orientation polarization arises when there is a permanent dipole moment in the material. Materials such as HCl and H_2O will have a net permanent dipole moment because the charge distributions of these molecules are skewed. For example, in a HCl molecule, the chlorine atom will be negatively charged and the hydrogen atoms will be positively charged causing the molecule to be dipolar. The dipolar nature of the molecule should cause a dipole moment in the material, however, in the absence of an electric field, the dipole moment is canceled out by thermal agitation resulting in a net zero dipole moment per molecule. When an electric field is applied however, the molecule will begin to rotate to align the molecule with the field, causing a net average dipole moment per molecule as shown in figure 2.9.
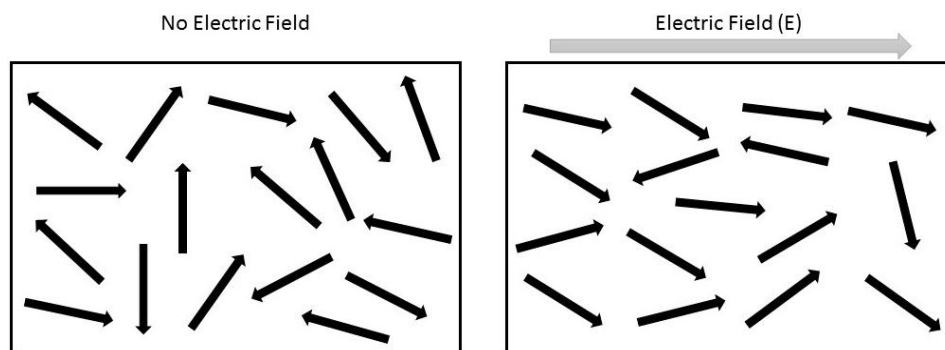
Figure 2.9: Orientation or Dipolar polarization

2.8.2.4   Interfacial or Space charge Polarization

Interfacial or space charge polarization occurs when there is an accumulation of charge at an interface between two materials or between two regions within a material because of an external field. This can occur when there is a compound dielectric, or when there are two electrodes connected to a dielectric material. This type of electric polarization is different from orientation and ionic polarization because instead of affecting bound positive and negative charges i.e. ionic and covalent bonded structures, interfacial polarization also affects free charges as well. As a result interfacial polarization is usually

observed in amorphous or polycrystalline solids. Figure 2.10 shows an example of how free charges can accumulate in a field, causing interfacial polarization. The electric field will cause a charge imbalance because of the dielectric material's insulating properties. However, the mobile charges in the dielectric will migrate over maintain charge neutrality. This then causes interfacial polarization.
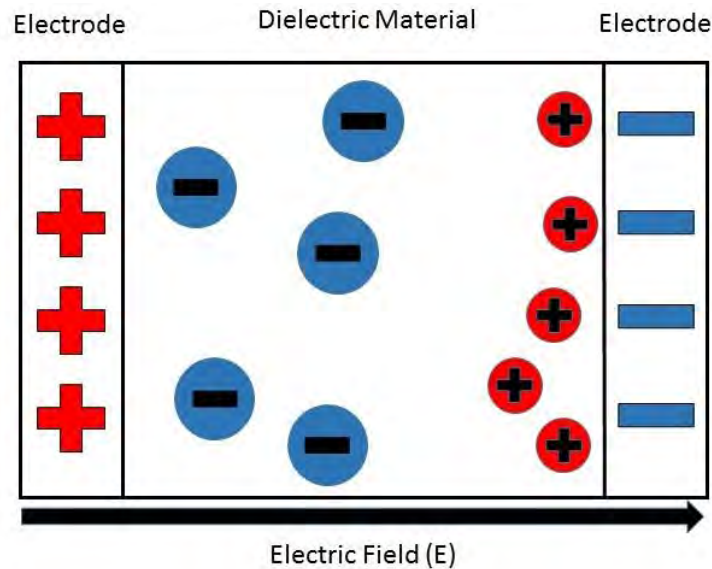
Figure 2.10: Interfacial or Space charge polarization

2.8.3   Dielectric properties

Studies of dielectric properties provide a great deal of information about the acceptance of material for various applications. Dielectric constant (ε'), dielectric loss (tan δ) are important parameters for dielectric materials.

2.8.3.1 iDelectric constant

iDelectric constant**,** property of an electrical insulating material (a dielectric) equal to the ratio of the capacitance of a capacitor filled with the given material to the capacitance of an identical capacitor in a vacuum without the dielectric material. The insertion of a dielectric between the plates of, say, a parallel-plate capacitor always increases its capacitance, or ability to store opposite charges on each plate, compared with this ability

when the plates are separated by a vacuum. If C is the value of the capacitance of a capacitor filled with a given dielectric and C_o is the capacitance of an identical capacitor in a vacuum, the dielectric constant, symbolized by ε', is simply expressed as $\varepsilon' = C/C_o$. E is always less than or equal to E_o, so the dielectric constant is greater than or equal to 1. The larger the dielectric constant, the more charge can be stored. Completely filling the space between capacitor plates with a dielectric increases the capacitance by a factor of the dielectric constant: $C = \varepsilon' \, C_o$, where C_o is the capacitance with no dielectric between the plates. For a parallel-plate capacitor containing a dielectric that completely fills the space between the plates, the capacitance is given by:

$$\varepsilon' = \frac{C \times d}{\varepsilon_o \times A}$$ (2.3)

where C Dsthe measured capacDatace of the sample, d DsthIDkness of the capacDtr Dn meters and A   Dsthe area of cross sectIDn of the dDskspace sample and ε_o ID the permDtIDDy of the free space (8.854×10^{-12} F/m).

2.8.3.2 Dielectric loss

iDelectric loss, loss of energy that goes into heating a dielectric material in a varying electric field. For example, a capacitor incorporated in an alternating-current circuit is alternately charged and discharged each half cycle. During the alternation of polarity of the plates, the charges must be displaced through the dielectric first in one direction and then in the other, and overcoming the opposition that they encounter leads to a production of heat through dielectric loss, a characteristic that must be considered when applying capacitors to electric circuits. Dielectric loss quantifies a dielectric material's inherent dissipation of electromagnetic energy into, e.g., heat. It can be parameterized in terms of either the loss angle δ or the corresponding loss tangent tan δ.

2.9 Why BiFeO$_3$

Among compounds that are multiferroics, BiFeO$_3$ (BFO) is paradigmatic and currently the most studied material for novel applications which allow mutual control of the electric polarization with magnetic field and magnetization by an electric field [40].is ferroelectric below $T_C \sim 1103$ K and antiferromagnetic below $T_N \sim 643$ K. In fact,

$BiFeO_3$ is the only prototype which shows both ferromagnetism and ferroelectricity in a single crystal above room temperature. The ions responsible for the production of ferroelectricity and magnetism are Bi^{3+} and Fe^{+3} ions. Ferroelectricity is produced due to Bi^{3+} and antiferromagnetism is due to Fe^{+3} ions. $BiFeO_3$ shows anti-ferromagnetic G-type spin configuration along the $[111]_c$ or $[001]_h$ directions in its pseudocubic or rhombohedral structure. $BiFeO_3$ has a superimposed incommensurate cycloid spin structure with a periodicity of 620 Å along the $[110]_h$ axis at room temperature. This structure cancels the macroscopic magnetization and inhibits observation of the linear ME effect in the bulk $BiFeO_3$. The decrease in particle size has been proved to be effective in suppressing this cycloid structure and enhancing the magnetic moment of $BiFeO_3$ as a result of their low dimensionality and quantum confinement effect. Interestingly, this ferromagnetic $BiFeO_3$ exhibits characteristic features in dielectric properties around the magnetic transition temperature, highlighting useful multiferroic behavior [41].

2.10 Why nanoparticles

The term 'nanoparticle' is used to describe a particle with size in the range of 1 to 100 nm, at least in one of the three dimensions. Nanoparticles are of great scientific interest as they are, in effect, a bridge between bulk materials and atomic or molecular structures. A bulk material should have constant physical properties regardless of its size, but at the nano-scale size-dependent properties are often observed.

Thus, the properties of materials change as their size approaches the nanoscale and as the percentage of atoms at the surface of a material becomes significant. The interesting and sometimes unexpected properties of nanoparticles are therefore largely due to the large surface area of the material. Because for a spherical particle, the surface to volume ratio (S/V) is inversely proportional to its radius (R).

Because

$$S/_V = 4\pi R^2 /\frac{4}{3}\pi R^3 = 3/_R$$

The high surface area to volume ratio of nanoparticles provides a tremendous driving force for diffusion, especially at elevated temperatures. Nanoparticles often possess unexpected optical properties as they are small enough to confine their electrons and produce quantum effects [42]. Absorption of solar radiation is much higher in materials composed of nanoparticles than it is in thin films of continuous sheets of material.

Metal, dielectric, and semiconductor nanoparticles have been formed, as well as hybrid structures (e.g., core–shell nanoparticles) [43]. Nanoparticles made of semiconducting material may also be labeled quantum dots if they are small enough (typically sub 10 nm). Such nanoscale particles are used in biomedical applications as drug carriers or imaging agents.

Semi-solid and soft nanoparticles have been manufactured. A prototype nanoparticle of semi-solid nature is the liposome. Various types of liposome nanoparticles are currently used clinically as delivery systems for anticancer drugs and vaccines.

Nanoparticles with one half hydrophilic and the other half hydrophobic are termed Janus particles and are particularly effective for stabilizing emulsions. They can self-assemble at water/oil interfaces and act as solid surfactants.

The magnetic response of $BiFeO_3$ nanoparticles greatly increases for samples below 62 nm as compared with the bulk. The relative proportion of uncompensated spins at the surface becomes larger with decreasing particle size. Hence, the nanoparticles show size-dependent magnetic behavior according to confinement effects with enhanced magnetic behavior at nano-level.

2.11 Crystal Structure of $BiFeO_3$ (BFO)

$BiFeO_3$ has rhombohedrally distorted perovskite structure belonging to the space group of R3c with lattice parameters of a_{hex} = 5.571Å and c_{hex} = 13.868Å at room temperature [44].
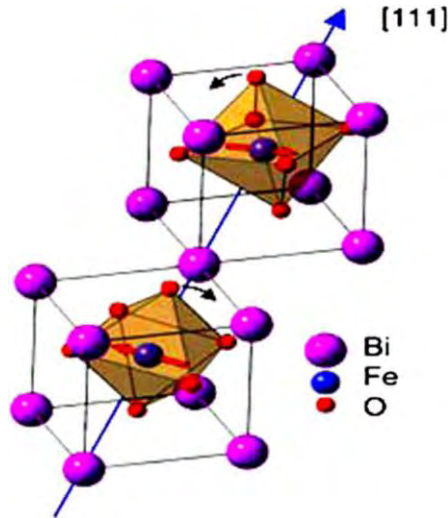
Figure 2.11: Crystal structure of $BiFeO_3$ (BFO)

The corner positions are occupied by Bi ions, at the center of the cube lies the transition Fe ion and the face centers are occupied by the oxygen ions. In such a distorted structure, the *R3c* symmetry permits the development of spontaneous polarization (P_s). The Fe-O-Fe angle controls the magnetic exchange and orbital overlap between Fe and O, and as such it determines the magnetic ordering temperature and the conductivity.

The BFO unit cell can be described both in the hexagonal and in the pseudo-cubic form figure 2.12. The pseudo-cubic representation of these rhombohedral cell parameters is a_c = 3.963 Å. The space group is determined as *R3c* with six formula units per hexagonal unit cell or two formula units per pseudo-cubic unit cell. In this structure, the pseudo-cubic $[1\ 1\ 1]_c$ is equivalent to hexagonal $[0\ 0\ 1]_h$ [40].
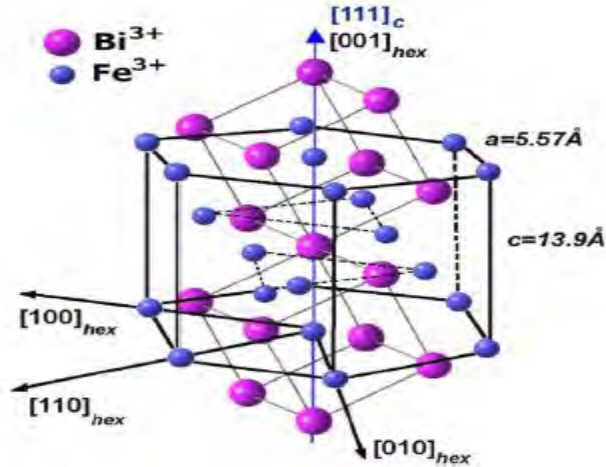
Figure 2.12: BFO unit cell in the pseudo-cubic form.

2.11.1 Magnetism in $BiFeO_3$

Sosnowska *et al* [45] studied the BFO magnetic structure and showed that each Fe^{3+} spin is surrounded by six anti parallel spins on the nearest Fe neighbors which is known as G-type antiferromagnetism. The exchange interaction between neighboring Fe magnetic moments within the $(0\,0\,1)_h$ planes is ferromagnetic and antiferromagnetic along $[0\,0\,1]_h$ [46]. The $R3c$ symmetry also permits a canting of the antiferromagnetic sub lattice resulting in a weak ferromagnetism if magnetic moments of Fe^{3+} are oriented perpendicular to the $[0\,0\,1]_h$ axis [46].
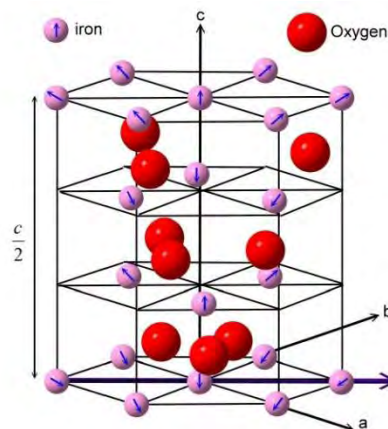
Figure 2.13: Hexagonal structure of $BiFeO_3$ lattice with Fe^{3+} and O_2-ions. The arrows indicate direction of Fe spins.

However, it was observed that the antiferromagnetic spin structure of BFO is modified by a long range modulation of 64 nm leading to a spin cycloid structure, also known as spiral modulated spin structure (SMSS) [45]. This spiral modulated spin structure leads to cancellation of any macroscopic magnetization.
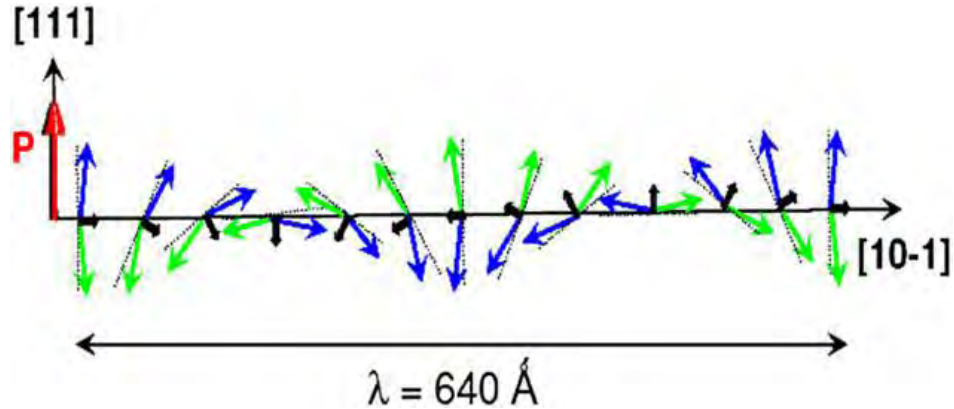
Figure 2.14: Schematic representation of the spin cycloid. The canted anti-ferromagnetic spins (blue and green arrows) give rise to a net magnetic moment (purple arrows) that is averaged out to zero due to the cycloidal rotation. The spins are contained within the plane defined by the polarization vector (red) and the cycloidal propagation vector (black) [47].

2.11.2 Ferroelectricity in BiFeO$_3$

The origin of ferroelectricity in BFO can be understood its highly distorted perovskite structure with rhombohedral symmetry and space group *R3c* .In such a distorted perovskite structure, *R3c* symmetry allow spontaneous polarization (P$_s$) along the pseudocubic [111] direction [48] . Because the ferroelectric state is attributed to a large displacement of the Bi ions relative to the FeO$_6$ octahedra, this leads to the following important consequence. The ferroelectric polarization of BFO lies along the [111] direction, leading to the formation of eight possible polarization directions (positive and negative orientations along the four cube diagonals, Pi ± with i= {1, 4}) which correspond to four structural variants (Figure 2.15).
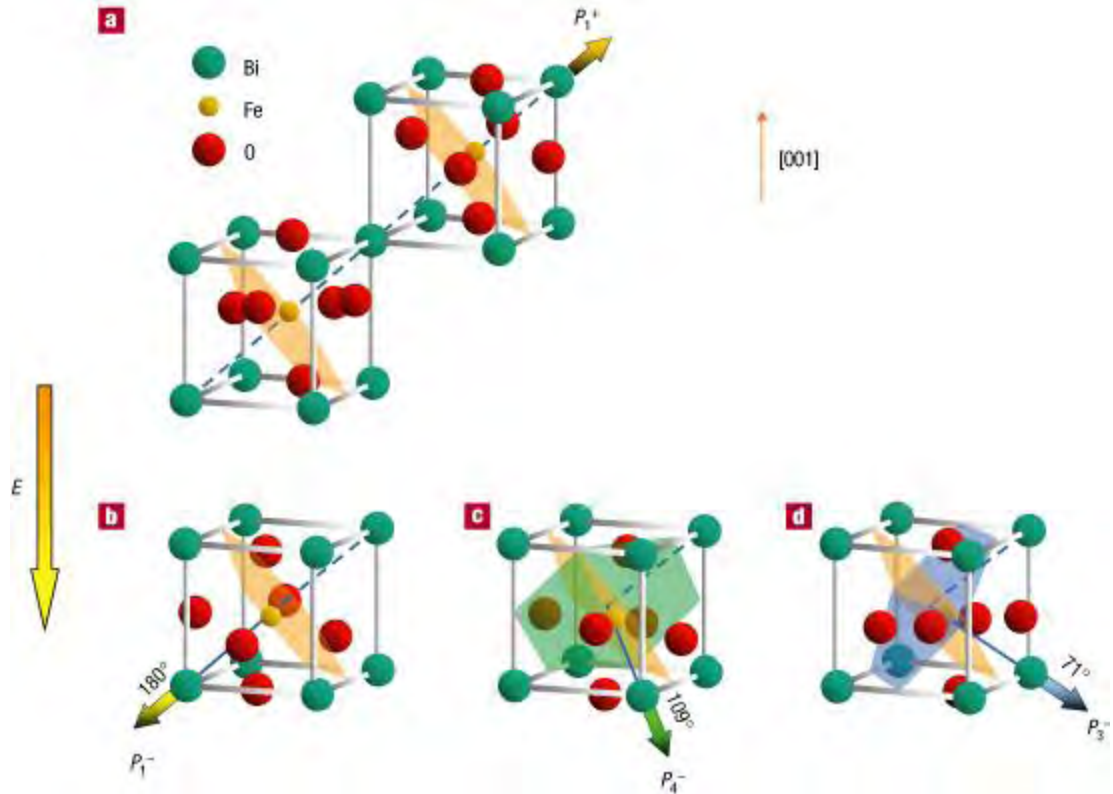
Figure 2.15: Schematic of crystal structure of BFO and ferroelectric polarization (arrow) and antiferromagnetic plane (shaded planes).

Whether A site or B site would get polarized depends on Goldschmid Tolerance Factor,

$$t = (r_{Bi} + r_O)/\sqrt{2}(r_{Fe} + r_O) .$$

If $t < 1$ the oxygen octahedral must bunckle to fit in the unit cell.

For $BiFeO_3$ $t = (1.17 + 1.28)/\sqrt{2}(0.69 + 1.28)$ =0.88, thus buckling of FeO_6 occurs which confirms A site polarization. Because buckling of FeO_6 is the main cause behind A site polarization.

2.11.3 BiFeO₃ (Bismuth Ferric Oxide) as Photocatalyst

2.11.3.1 Photocatalysis

Semiconductor photocatalysis, which provides a promising method for the chemical conversion of solar energy, has been the many research focus because of its application for the destruction of chemical contaminants and water splitting [49]. The basic principle of the semiconductor photocatalysis involves photo generated electrons ($e-$) and holes ($h+$) that migrate to the surface acting as redox sources for the destruction of the pollutants when a high energy incident light (photon energy) irradiated on the semiconductor surface and causing excitation of the charge carriers in the semiconductor. Photons of sufficient energy ($> E_{gap}$) are needed to excite e- & h+ pairs across the band gap. The photo-generated electrons and holes can take part in the REDOX chemical reactions as shown in the illustration below (Figure 2.16) [50].
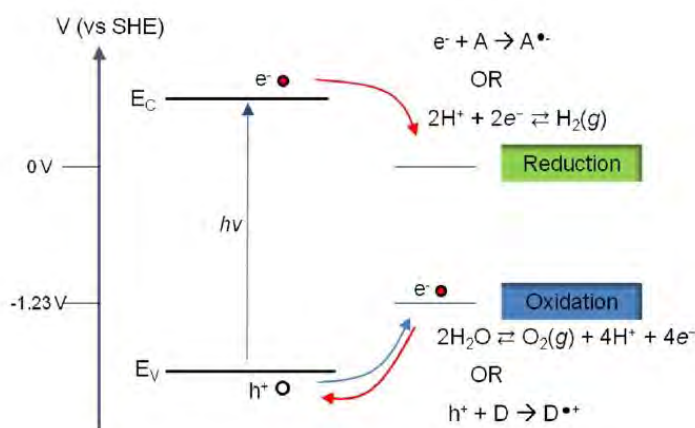
Figure 2.16: REDOX reactions from the photo-generated electrons and holes.

There are a few scenarios that would take place for photogenerated electrons in conduction-band: (1) it can combine with the holes in valence-band and dissipate the energy as heat, or (2) the photogenerated electrons get trapped in metastable surface states, or (3) react with charge species (electron donors and electron acceptors) that adsorbed on the semiconductor surface or within the vicinity of electrical double layer of the charged particles. The valence band holes are powerful oxidants (+1.0 to +3.5V vs NHE depending on the semiconductor and pH), while the conduction-band electrons are

good reductants (+0.5 to -1.5V vs NHE). If there is a suitable scavenger or surface defect state available to trap the electron or hole, recombination is prevented and redox reactions may occur. The photogenerated electrons and holes will recombine within a few nanoseconds and dissipate the stored energy if there is no suitable electron and hole scavengers. Most organic photodegradation reactions utilize the oxidizing power of the holes either directly or indirectly.

References:

[1] Maxwell, J. C., "A Dynamical Theory of the Electromagnetic Field", Phil. Trans. R. Soc. L., 155, 459, 1865.

[2] Landau, L. D., Lifshitz, E. M., Electrodynamics of continuous media (Fizmatlit, Moscow, 1959)

[3] Schmid, H., "Multi-ferroic magnetoelectrics, Ferroelectrics", 162, 317, 1994.

[4] Eerenstein, W., Mathur, N. D., Scott, J. F., "Multiferroic and magnetoelectric materials", Nature, 442, 759, 2006.

[5] Ascher, E., Rieder, H., Schmid, H., and Stössel, H., "Some properties of ferromagnetoelectric nickeliodine boracite, $Ni_3B_7O_{13}I$", J. App. Phys., 37, 1404, 1966.

[6] Nicola., Hill, A., "Why are there so few magnetic ferroelectrics?", J. Phys. Chem. B., 104, 6694, 2000.

[7] Wang, J., Neaton, J. B., Zheng, H., Nagarajan, V., Ogale, S. B., Liu, B., Viehland, D., Vaithyanathan, V., Schlom, D. G., Waghmare, U. V., Spaldin, N. A., Rabe, K. M., Wuttig, M., and Ramesh, R., "Epitaxial $BiFeO_3$ multiferroic thin film heterostructures", Science, 299, 1719, 2003.

[8] Kimura, T., Goto, T., Shintani, H., Ishizaka, K., Arima., Tokura, Y., "Magnetic control of ferroelectric polarization", Nature, 426, 55, 2003.

[9] Hur, N., Park, S., Sharma, P. A., Ahn, J. S., Guha, S., Cheong, S-W., "Electric polarization reversal and memory in a multiferroic material induced by magnetic fields", Nature, 429, 392, 2004.

[10] Fiebig, M., "Revival of the magnetoelectric effect", J. Phys. D: Appl. Phys., 38, 123, 2005.

[11] Khomskii, D. I., "Multiferroics: Different ways to combine magnetism and ferroelectricity", J. Magn. Magn. Mater., 306, 1, 2006.

[12]. Cheong, S.-W., and Mostovoy, M., "Multiferroics: a magnetic twist for ferroelectricity", Nature Mater., 6, 13, 2007.

[13] Velev, J. P., Jaswal, S. S., Tsymbal, E. Y., "Multiferroic and magnetoelectric materials and interfaces", Math., Phys. Eng. Soc., 369, 3069, 2011.

[14] Prellier, W., Singh, M., Murugavel, P., "The single-phase multiferroic oxides: from bulk to thin film", J. Phys.: Condens. Matter, 17, 803, 2005.

[15] Tokura, Y., Kida, N., "Dynamical magnetoelectric effects in multiferroic oxides", Math., Phys. Eng. Soc., 369, 3679, 2011.

[16] Lawes, G., Srinivasan, G., "Introduction to magnetoelectric coupling and multiferroic films", J. Phys. D: Appl. Phys., 44, 243001, 2011.

[17] Ma, J., Hu, J., Li, Z., and Nan, C.-W., "Recent Progress in Multiferroic Magnetoelectric Composites: from Bulk to Thin Films", Adv. Mater., 23, 1062, 2011.

[18] Martin, L. W., Crane, S. P., Chu, Y.-H., Holcomb, M. B., Gajek, M., Huijben, M., Yang, C. H., Balke, N., and Ramesh, R., "Multiferroics and magnetoelectrics: thin films and nanostructures", J. Phys.: Condens. Matter, 20, 434220, 2008.

[19]. Nan, C. W., Bichurin, M. I., Dong, S., Viehland, D., Srinivasan, G., "Multiferroic magnetoelectric composites: Historical perspective, status, and future directions", J. Appl. Phys., 103, 031101, 2008.

[20]. Srinivasan, G., "Magnetoelectric Composites", Ann. Rev. Mater. Res., 40, 153, 2010.

[21] Zhai, J., Xing, Z., Dong, S., Li, J., and Viehland, D., "Magnetoelectric Laminate Composites: An Overview", J. Am. Ceram. Soc., 91, 351, 2008.

[22] Martin, L., Chu, Y.-H., and Ramesh, R., "Advances in the growth and characterization of magnetic, ferroelectric, and multiferroic oxide thin films", Mater. Sci. Eng.: R: Reports, 68, 89, 2010.

[23] Yan, L., Yang, Y., Wang, Z., Xing, Z., Li, J., Viehland, D., "Review of magnetoelectric perovskite-spinel self-assembled nano-composite thin films", J. Mater. S., 44, 5080, 2009.

[24] Khomskii, D., "Classifying multiferroics: Mechanisms and effects", Physics, 2, 20, 2009.

[25] Valasek, J., "Piezoelectric and allied phenomena in Rochelle salt", Phys. Rev., 17, 475, 1921.

[26] Duan, F., Guojan, J., "Introduction to Condensed Matter Physics", World Scientific 1, Singapore, 2005.

[27] Kittel, C., "Introduction to solid state Physics", Am. J. Phys., 35, 547, 1967.

[28]. Hall, J. R., Hook, H. E., "Solid state physics (2nd ed.)", 205, 1994.

[29]. David Jiles., "Introduction to Magnetism and Magnetic Materials", 1st edition, Chapman & Hall, New York, 1991.

[30] Omar, M. Ali., "Elementary Solid State Physics: Principles and Applications", Addition Wesley Publishing Company, Inc., 2003.

[31] Abrahams, S. C., "FERROELASTICITY", Mat. Res. Bull., 6, 881, 1971.

[32] Salje, Ekhard, K. H., "Ferroelastic Materials" Annu. Rev. Mater. Res., 42, 265, 2012.

[33] Salje, E., Hoppmann, G., "Direct observation of ferroelasticity in $Pb_3(PO_4)_2$-$Pb_3(VO_4)_2$", Mat. Res. Bull., II, 1545, 1976.

[34] Parkin, S. S. P., Hayashi, M., Thomas, L., "Magnetic domain-wall racetrack memory", Science, 320, 190, 2008.

[35] Cowburn, R. P., Welland, M. E., "Room temperature magnetic quantum cellular automata", Science 287, 1466, 2000.

[36] Saxena, A. Lookman, T., "Magnetic symmetry of low-dimensional multiferroics and ferroelastics", Phase Trans., 84, 421, 2011.

[37] Schmid, H., "On ferrotoroidics and electrotoroidic, magnetotoroidic and piezotoroidic effects", Ferroelectrics, 252, 41, 2001.

[38] Spaldin, N. A., Fiebig, M., and Mostovoy, M., "The toroidal moment in condensed-matter physics and its relation to the magnetoelectric effect", J. Phys.: Condens. Matter, 20, 434203, 2008.

[39] Carter, C. B., Norton, M. G., "Ceramic Materials Science and Engineering", Springer, New York, 2007.

[40] Lazenka, V. V., Zhang, G., Vanacken, J., Makoed, I. I., Ravinski, A. F. and Moshchalkov, V. V., "Structural transformation and magnetoelectric behaviour in $Bi_{1-x}Gd_xFeO_3$ multiferroics", J. Phys. D: Appl. Phys., 45, 125002, 2012.

[41] Mazumder, R., Devi, P. S., Bhattacharya, D., Choudhury, P., Sen, A. and Raja, M., "Ferromagnetism in nanoscale $BiFeO_3$", Appl. Phys. Lett., 91, 062510, 2007.

[42] Hewakuruppu, Y. L., Dombrovsky, L. A., Chen, C., Timchenko, V., Jiang, X., Baek, S., and Taylor R. A. "Plasmonic "pump–probe" method to study semi-transparent nanofluids", Applied Optics, 52, 6041, 2013.

[43] Robert, T., Sylvain, C., Todd, O., Patrick, P., Andrey, G., Wei, L., Gary, R., Ravi, P., Himanshu, T., "Small particles, big impacts: A review of the diverse applications of nanofluids", J. Appl. Phys., 113, 011301, 2013.

[44] Cataln, G., Scott, J. F., "Physics and applications of bismuth ferrite", Adv. Mater., 21, 2463, 2009.

[45] Sosnowska, I., Neumaier, T. P., Steichele, E., "Spiral magnetic ordering in bismuth ferrite", J. Phys. C: Solid State Phys., 15, 4835, 1982.

[46] Ederer, C., Spaldin, N. A., "Weak ferromagnetism and magnetoelectric coupling in bismuth ferrite", Phys. Rev. B., 71, 060401, 2005.

[47] Catalan, G., Scott, J. F., "Physics and Applications of Bismuth Ferrite", Adv. Mater., 21, 2463, 2009.

[48] Porporati, A. A., Tsuji, K., Valant, M., Axelsson, A. K., Giuseppe, P., "Raman tensor elements for multiferroic $BiFeO_3$ with rhombohedral R3c symmetry", J. Raman Spectrosc., 41, 84, 2010.

[49] Hoffmann, M. R., Martin, S. T., Choi, W., Bahnemann, D. W., "Environmental Applications of Semiconductor Photocatalysis", Chem. Rev., 95, 69, 1995.

[50] Fox, M. A., Dulay, M. T., "Heterogeneous Photocatalysis", Chem. Rev., 93, 341, 1993.

Chapter 3

Sample Preparation and
Experimental Techniques

3.1 Introduction

Different methods have been adopted for preparing the $BiFeO_3$ nanopowder. Recently, wet chemical methods [1] have received abundant attention. Among the wet chemical methods the modified Pechini sol-gel method is very cost effective, simple and suitable for synthesis of homogenous and crystalline nanopowder. The process is based on the mixing of reactants that oxidize easily, such as metal nitrates, and an organic chelating agent that acts as reducing agent.

3.1.1 Sol-Gel methods

The sol-gel process may be described as:

"Formation of an oxide network through polycondensation reactions of a molecular precursor in a liquid".

A **sol** is a stable dispersion of colloidal particles or polymers in a solvent. The particles may be amorphous or crystalline. An aerosol is particles in a gas phase, while a sol is particles in a liquid.

A **gel** consists of a three dimensional continuous network, which encloses a liquid phase, in a colloidal gel, the network is built from agglomeration of colloidal particles. In a polymer gel the particles have a polymeric sub-structure made by aggregates of sub-colloidal particles. Generally, the sol particles may interact by van der Waals forces or hydrogen bonds. A gel may also be formed from linking polymer chains. In most gel systems used for materials synthesis, the interactions are of a covalent nature and the gel process is irreversible. The gelation process may be reversible if other interactions are involved.

The advantages of sol-gel synthesis as the prime method for the production of $BiFeO_3$ are:

- Multi component compounds may be prepared with a controlled stoichiometry mixing sols of different compounds.
- The sol-gel method prevents the problems with co-precipitation, which inhomogeneous be a gelation reaction.
- Self-purification due to the high exothermic temperatures involvement.
- Synthesis of single phase materials at very low temperatures.
- Simple and cost effective.
- Enables mixing at an atomic level.
- Formation of nanopowder in the desired size and shape with uniform particle size distribution.

3.2 Optimizing synthesis route and parameter:

As stated in section 1.2, one of the aims of this thesis is to synthesize nanocrystalline $BiFeO_3$ with uniform and homogenous particle size distribution. At very beginning conventional Pechini sol-gel route was adopted to synthesize $BiFeO_3$ nanoparticles using $Bi(NO_3)_3.5H_2O$ and $Fe(NO_3)_3.9H_2O$ as the initial components, 2-methoxyethanol as the solvent, NH_4OH as pH controller, acetic acid CH_3COOH as a chelating agent and ethylene glycol ($OHCH_2CH_2OH$) as a polymerizing agent.

3.2.1 Synthesis Procedure (Pechini sol-gel route)

- ❖ Calculated amount of $Bi(NO_3)_3.5H_2O$ and $Fe(NO_3)_3.9H_2O$ were initially taken into a beaker with about 200-250 ml 2-methoxyethanol as the solvent.
- ❖ Then the solution was magnetically stirred for about 4 hour until all the components get dissolved and the clear solution was obtained (Figure 3.1a).
- ❖ Then the pH of the solution was increased to 5 by adding NH_4OH. The color of the solution turned to blackish red from red and finally to nontransparent whitish red color (Figure 3.1b).
- ❖ Afterwards acetic acid (CH_3COOH) and ethylene glycol ($OHCH_2CH_2OH$) in 1:1 molar ratio were added to the solution sequentially.

❖ After that the solution was heated at constant temperature at about 70 °C to 80 °C with continuous magnetic stirring for about 30 to 32 hours (Figure 3.1c).

❖ At the end almost all the solvent got evaporated and the solution got thicker and a thin gel like layer of dark brown color appeared (Figure 3.1d).
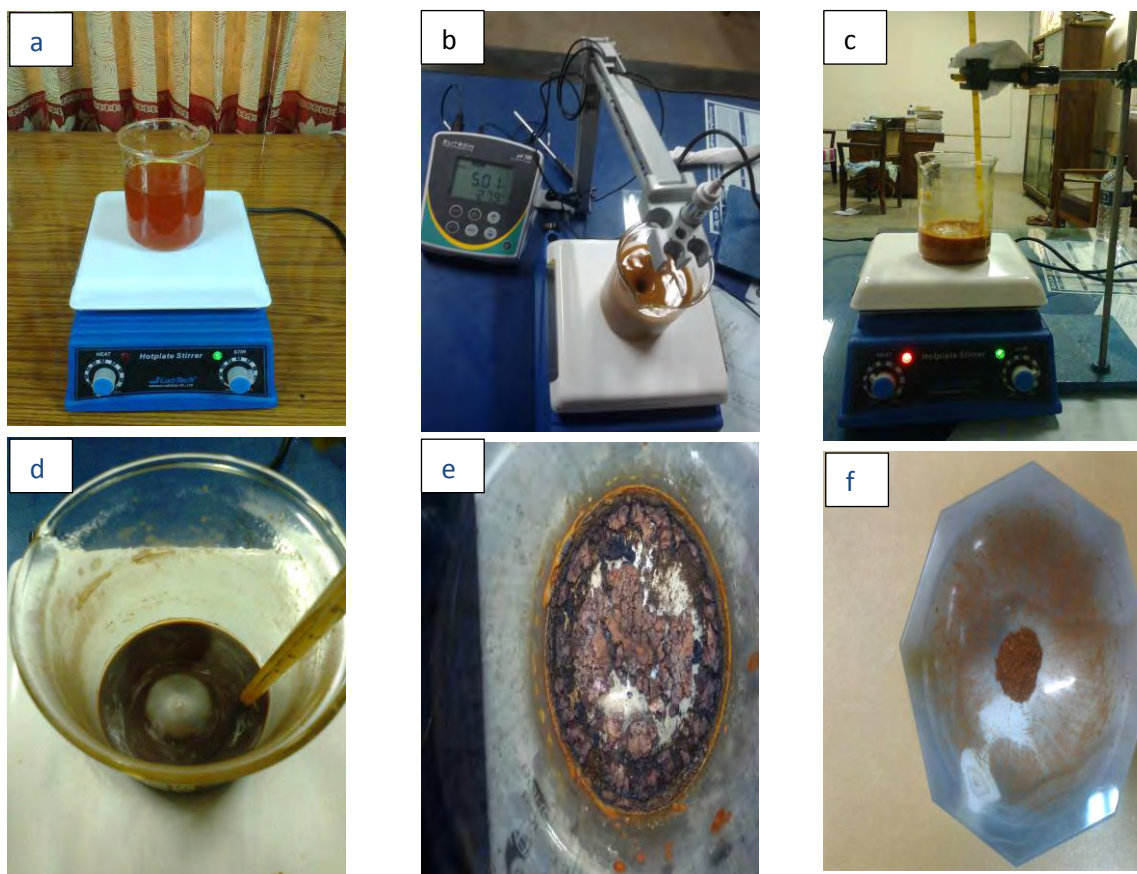
Figure 3.1: Synthesis steps a) Dissolving components with 4 hours continuous stirring b) Solution after pH control c) Solution during heating at about 70 °C to 80 °C d) Onset of a thin gel like layer e) Dried gel after oven heating f) After final grinding.

❖ Then the sample was dried in an oven for about 28 hours at 120 °C temperature with two or three intermediate grinding, one after the 1ˢᵗ 12 hours heating and the other two at an interval of 4 hours. The intermediate grinding ensures proper esterification and uniform drying (Figure 3.1 e).

❖ The dried gel was then grinded into powder in the mortar.

❖ The obtained powder was then annealed for 2 hours at 400 ^{o}C, 500 ^{o}C and 600 ^{o}C temperatures. The heating and cooling rate of the furnace were maintained at 3 °C/min.

❖ Finally the powder was grounded to get $BiFeO_3$ nanoparticles (Figure 3.1f).

3.2.2 Flow Chart of Synthesis Procedure:

Mixing of $Bi(NO_3)_3.5H_2O$ and $Fe(NO_3)_3.9H_2O$ in about 200-250 ml 2-methoxyethanol

Continuously stirred for about 4 hours

The pH of the solution was increased to 5 by adding NH_4OH

Addition of acetic acid (CH_3COOH) and ethylene glycol ($OHCH_2CH_2OH$) in 1:1 molar ratio

Heating at constant temperature at about 70 ^{o}C to 80 ^{o}C with continuous magnetic stirring for about 30 to 32 hours.

Appearance of a thin gel like layer of dark brown color.

Drying in the oven for about 28 hours at 120 ^{o}C temperature with two or three intermediate grinding

Grinded into powder in the mortar

Annealing for 2 hours at 400 °C, 500 °C and 600 °C temperatures

Final grinding to obtain the $BiFeO_3$ nanoparticles

The FESEM image of the synthesized particles by using the above mentioned route and chemicals are shown below:
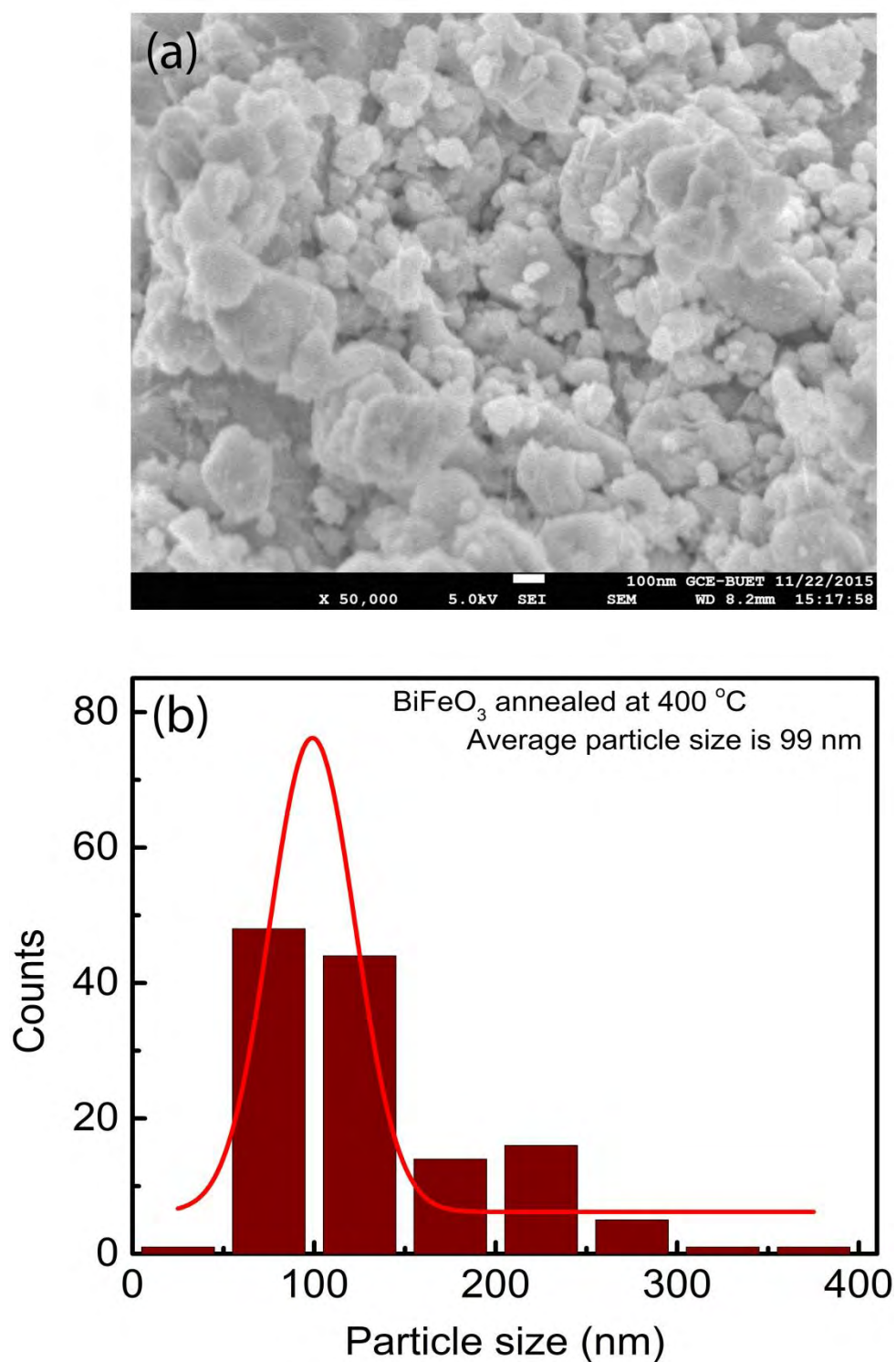
Figure 3.2: (a) FESEM image, (b) particle size distribution of $BiFeO_3$ (400 ^{o}C)

From the FESEM image it can be seen that, the particles are mostly agglomerated and not homogeneous in size. By using this synthesis route, the calculated average particle size is 99 nm. The size of the synthesized particles is not in desired range which is around 62 nm, the wavelength of spiral modulated spin structure of $BiFeO_3$.

In order to get homogeneous and required size nanoparticles, the synthesis route was changed and optimized. In this new route, deionized water was used as solvent instead of 2-methoxyethanol and citric acid as chelating agent instead of acetic acid. Because previous literature reports that, citric acid is stronger chelating agent than acetic acid and by using deionized water as solvent and citric acid as chelating agent it is expected to get homogeneous and small size nanoparticles [2].

3.2.3 New Synthesis Procedure (modified Pechini sol-gel route)

❖ Stoichiometric proportion of $Bi(NO_3)_3.5H_2O$ and $Fe(NO_3)_3.9H_2O$ were initially dissolved in 400 ml deionized water with an individual concentration of 0.025M.

❖ The solution was stirred for about half an hour to obtain a clear solution.

❖ When the solution was transparent, 0.02 mole of $C_6H_8O_7$ as the chelating agent was added to the solution to complex the metal cations (Figure 3.3a).

❖ The solution was then stirred and heated at 70-75 °C for 8-10 hours to form a transparent blackish-red sol (Figure 3.3b).

❖ Afterwards appropriate amount of ethylene glycol was added to the solution as polymerization agent.

❖ The resultant solution was heated at 70-75 °C to initiate the polymerization reaction and a few minutes later a gel was formed with vigorous boiling and fuming (Figure 3.3c).
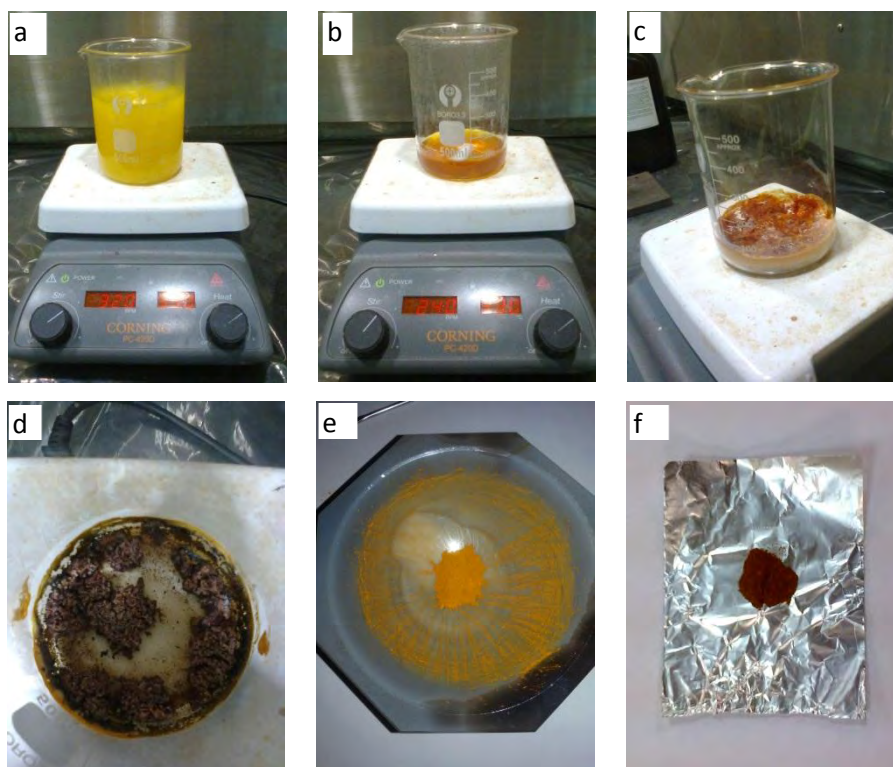
Figure 3.3: Synthesis steps a) mixing raw materials into deionized water, b) formation of sol, c) formation of gel, d) precursor xerogel, e) ground xerogel, f) annealed $BiFeO_3$ powder.

- ❖ The gel was dried at 100 °C for 24 hours in a functional oven to obtain fluffy green xerogel (Figure 3.3d).
- ❖ The xerogel samples were then grounded into powder and annealed at 400-600 °C (the heating and cooling rate were maintained at 3 °C /min.) for 2 hours using a functional furnace in static air (Figure 3.3e).
- ❖ Finally the powders were grounded to get $BiFeO_3$ nanoparticles (Figure 3.3f).

3.2.4 New flow Chart of Synthesis Procedure:

Mixing of $Bi(NO_3)_3.5H_2O$ and $Fe(NO_3)_3.9H_2O$ in 400 ml deionized water with concentration of 0.025M .

Stirred half an hour

Addition of Citric acid

Heating and stirring at 70-75 °C with a magnetic stirrer for 8-10 hours to get red solution

Addition of ethylene glycol

The solution is heated at 70-75 °C to initiate the polymerization reaction and to get gel.

Drying at 100 °C for 24 hours

Fluffy green powder (xerogel)

Grinded into powder

Annealed for 2 hours at 400-600 °C temperatures

Final grinding to obtain the $BiFeO_3$ nanoparticles

The FESEM images (shown in chapter 4) of the synthesized powder by following this new route clearly demonstrated the formation of very fine homogenous and nearly spherical nanoparticles with very little agglomeration effect. The size and distribution of the nanoparticles prepared by using this new synthesis route was estimated. Their ferroelectric, ferromagnetic and optical characteristics will be presented in chapter 4.

3.2.5 Synthesis of Gd doped $BiFeO_3$ nanoparticles

The synthesis process of the Gd doped BFO powders was quite similar to the synthesis of pure BFO powder, except that there is an addition of rare earth metal (Gd) into the Bi-Fe ionic solution before the heating process.

3.2.6 Annealing

Annealing, in metallurgy and materials science, is a heat treatment that alters the physical and sometimes chemical properties of a material to increase its ductility and reduce its hardness, making it more workable. It involves heating a material to above its recrystallization temperature, maintaining a suitable temperature, and then cooling.

During annealing, atoms migrate in the crystal lattice and the number of dislocations decreases, leading to the change in ductility and hardness.

Laboratory Chamber Furnace (CAEBOLITE, ELF 11/6B / Germany) was used to anneal xerogel samples at 400 °C, 500 °C and 600 °C in air atmosphere. The basic annealing cycle in our experiment is shown in figure 3.5.

Figure 3.4: Furnace used for annealing xerogel sample
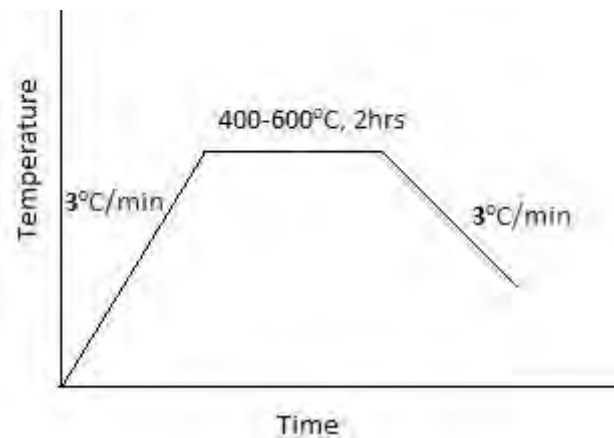
Figure 3.5: Annealing cycle

3.3 Characterization Techniques:

Our as prepared sample undergoes following characterization techniques:

- Field Emission Scanning Electron Microscope
- X- ray Diffraction Study
- Ferroelectric (P-E) measurements
- Dielectric property measurement
- SQUID Magnetometer
- UV-vis spectrophotometer

3.3.1 Field Emission Scanning Electron Microscope

Field Emission Scanning Electron Microscope (FESEM) is a type of microscope that works with electrons (particles with a negative charge) instead of light. These electrons are liberated from a field emission source. The object is scanned by electrons following a zig-zag pattern. A FESEM is used to visualize very small topographic details on the surface or entire or fractioned objects. By applying this technique it is possible to observe structures as small as 1 nanometer (= billion of a millimeter).

To observe morphology of the synthesized powders we used field emission scanning electron microscope, FESEM (JEOL JSM 7600F).

Figure 3.6: Field Emission Scanning Electron Microscope

In order to observe morphology of the synthesized powders, at first the powder sample was taken in a cupper tape which is actually consists of three layers, the lower one is a cupper layer, the middle one is a carbon tape and the upper one is the cupper tape where the sample was adhered. Then the sample was coated with platinum by ion sputtering method in auto fine coater for about 40 seconds. A 10 nm layer of platinum is coated upon the sample. Then the cupper tape is mounted on a holder in the specimen chamber and inserted in the FESEM.

Figure 3.7: JFC 1600 Auto Fine Coater

3.3.1.1 Scanning process and image formation

Electrons are liberated from a field emission source and accelerated in a high electrical field gradient. Within the high vacuum column these so-called primary electrons are focused and deflected by electronic lenses to produce a narrow scan beam that bombards the object. As a result secondary electrons are emitted from each spot on the object. The angle and velocity of these secondary electrons relates to the surface structure of the object. A detector catches the secondary electrons and produces an electronic signal. This signal is amplified and transformed to a video scan-image that can be seen on a monitor. The image obtained from FESEM analysis was used for morphological studies of the samples.

3.3.2: X- ray Diffraction Study

X-ray diffraction (XRD analysis) is a unique method in determination of crystallinity of a compound. This technique is primarily used for phase identification of a crystalline material and can provide information on unit cell dimensions.

Scattering of X-rays by the atoms of a crystal that produces an interference effect so that the diffraction pattern gives information on the structure of the crystal or the identity of a crystalline substance. This phenomenon is called X-ray diffraction. X-ray diffraction is now a common technique for the study of crystal structures and atomic spacing. XRD analysis is based on constructive interference of monochromatic X-rays and a crystalline sample.

X-ray diffractometer consist of three basic elements: an X-ray tube, a sample holder, and an X-ray detector.

Figure 3.8: X-ray Diffractometer (XRD)

X-rays are generated by a cathode ray tube by heating a filament to produce electrons, accelerating the electrons toward a target by applying a voltage, and bombarding the target material with electrons. When electrons have sufficient energy to dislodge inner shell electrons of the target material, characteristic X-ray spectra are produced. These spectra consist of several components, the most common being K_α and K_β. Copper is the most common target material for single-crystal diffraction, with CuK_α (λ= 1.5418 Å) radiation. Then the diffracted X-rays are filtered to produce monochromatic radiation, collimated to concentrate, and directed toward the sample. The interaction of the incident rays with the sample produces constructive interference (and a diffracted ray) when conditions satisfy Bragg's Law which is given by:

$$2d_{hkl} \sin \theta = n\lambda \qquad\qquad (3.1)$$

This law relates the wavelength (λ) of electromagnetic radiation to the diffraction angle (θ) and the lattice spacing (d_{hkl}) between two crystal plane in a crystalline sample. These diffracted X-rays are then detected, processed and counted. By scanning the sample through a range of 2θ angles, all possible diffraction directions of the lattice should be attained due to the random orientation of the powdered material.
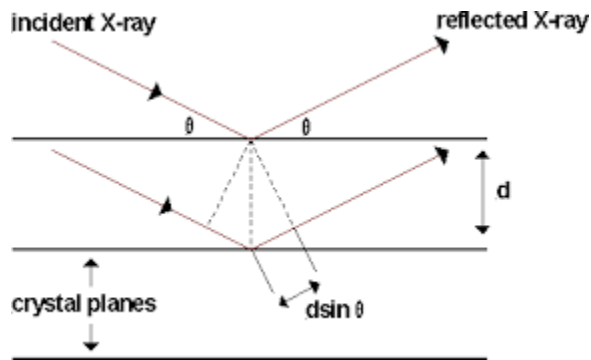
Figure 3.9: Bragg's law of diffraction

The intensity of diffracted X-rays is continuously recorded as the sample and detector rotate through their respective angles. A peak in intensity occurs when the mineral contains lattice planes with d_{hkl}-spacings appropriate to diffract X-rays at that value of θ. Once all d_{hkl}-spacings have been determined they are compared with standard data, available from the International Centre for Diffraction Data as the Powder Diffraction File (PDF), which facilitates to identify any impurity phases appeared as extra peaks.
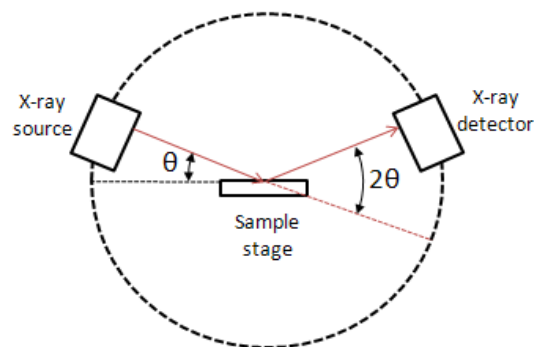
Figure 3.10: The schematic diagram shows the operation of XRD.

The average crystallite size (d) of the synthesized powders was calculated from the XRD patterns using the Scherrer formula which is given by:

$$d = \frac{K\lambda}{\beta \cos\theta} \qquad (3.2)$$

where k is the dimensionless shape factor with a typical value of about 0.94, λ is the X-ray wavelength, θ is the Bragg angle for the diffraction peak, β is the full width at half the maximum intensity (FWHM) of the corresponding diffraction peak.

3.3.3 Ferroelectric measurements

A ferroelectric measurement (Automatic P-E Loop tracer, MARINE INDIA) system (Figure 3.11) which was used for electrical characterization of synthesized materials. The system measured the hysteresis loops and leakage current for these materials. Measurements were performed at line frequency of 50 Hz.

The complete measurement system consists of the following:

- PE main unit
- Sample holder
- Furnace with temperature controller
- Desktop PC

Figure 3.11: Automatic P-E Loop tracer

3.3.3.1 Basic theory of operation

The basic PE test system is based on Sawyer Tower (S-T) circuit [3] (Figure 3.12).
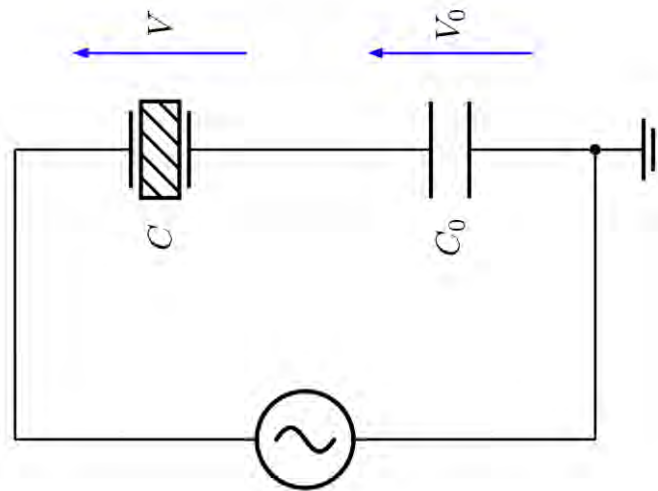
Figure 3.12: Sawyer Tower (S-T) circuit

The circuit consists of two capacitors, one due to sample (C) and other one is a linear known valued internal capacitor (C_o) they are connected in series. The principal is simple when two capacitors are connected in series and AC voltage is applied on both in series, the charge on both will be same. In order to get complete saturation the internal capacitance must be bigger that the sample capacitance.

3.3.4 Dielectric property measurement

A dielectric is an electrical insulator that may be polarized by the action of an applied electric field. When a dielectric materials is placed in an electric field, electric charge do not flow through the material, as in a conductor but only slightly shift from their average equilibrium positions causing dielectric polarization; positive charges are displaced along the field and negative charges shift in the opposite direction.

Dielectric typically means materials with a high polarizability. A common example of a dielectric is the electrically insulating material between the metallic plates of a capacitor. The polarization of the dielectric by the applied electric field increases the capacitor's surface charge for the given electric field strength.
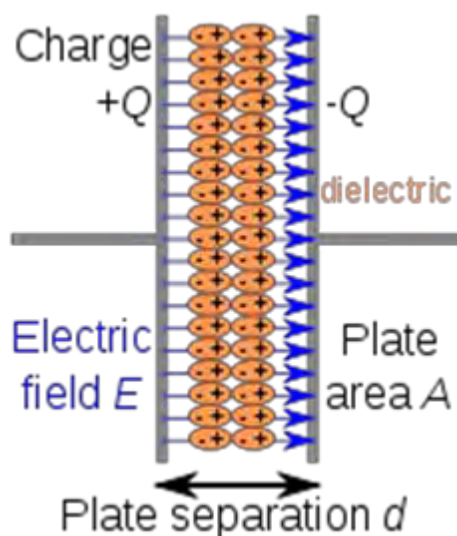
Figure 3.13: Diagram of dielectric plate

An impedance analyzer (WAYNE KERR 6500 B) was used to measure the dielectric property of samples. Measurements of the samples were done as a function of frequency and temperature.

First of all samples were prepared properly to measure dielectric properties correctly. Samples were kept clean and dry. They were polished with 120 grit paper in order to produce crack free solid sample. Samples were given geometrical shape commonly circular in order to measure the area. Sample thickness was kept quite uniform which was essential for correct measurement. For the measurement of dielectric properties the samples will be painted on either side with silver paste to ensure good electric contacts. Next the samples were kept in the holder of the impedance analyzer to measure the properties. The measure frequency was varied from 100Hz to 10MHz. Experimental set up is shown in figure 3.14.

Figure 3.14: WAYNE KERR impedance analyzer 6500B series

Measurements of dielectric properties normally involve the measurements of the change in capacitance and loss of a capacitor in presence of the dielectric materials. The behavior of a capacitance can now be described as follows. Here an ideal loss less air capacitor of capacitance C_o. On insertion of a dielectric material in a space the capacitance will be changed.The dielectric constant (ε_r) and electrical properties measurements on disk-spaced specimens will be carried out at room temperature on all the samples in the high frequency range. The dielectric constant ε' was calculated using the following relations:

$$\varepsilon' = \frac{C \times d}{\varepsilon_o \times A} \tag{3.3}$$

where C is the measured capaciatance of the sample, d is thickness of the capacitor in meters and A is the area of cross section of the disk space sample and ε_o is the permitivity of the free space (8.854×10^{-12} F/m) [4].

The dielectric constant depends strongly on the frequency of the alternating electric field and on the chemical structure, imperfection of the material, temperature and pressure.

3.3.5 SQUID Magnetometer

Superconducting Quantum Interference Device (SQUID) magnetometer is one of the most effective and sensitive ways of measuring magnetic properties. In particular, it is the only method which allows to directly determine the overall magnetic moment of a sample in absolute units. The superconducting quantum interference device (SQUID) consists of two superconductors separated by thin insulating layers to form two parallel Josephson junctions (figure 3.15).
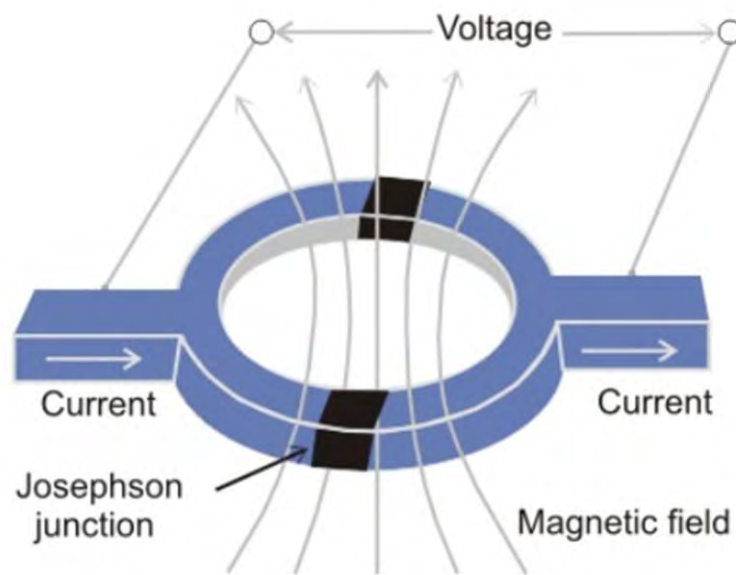
Figure 3.15: Josephson junctions

By Brian David Josephson in 1962, the electrical current density through a weak electric contact between two superconductors depends on the phase difference $\Delta\varphi$ of the two superconducting wave functions [5]. Moreover, the time derivative of $\Delta\varphi$ is correlated with the voltage across this weak contact. In a superconducting ring with two weak contacts, $\Delta\varphi$ is additionally influenced by the magnetic flux Φ through this ring. Therefore, such a structure can be used to convert magnetic flux into an electrical voltage. This is the basic working principle of a SQUID magnetometer.
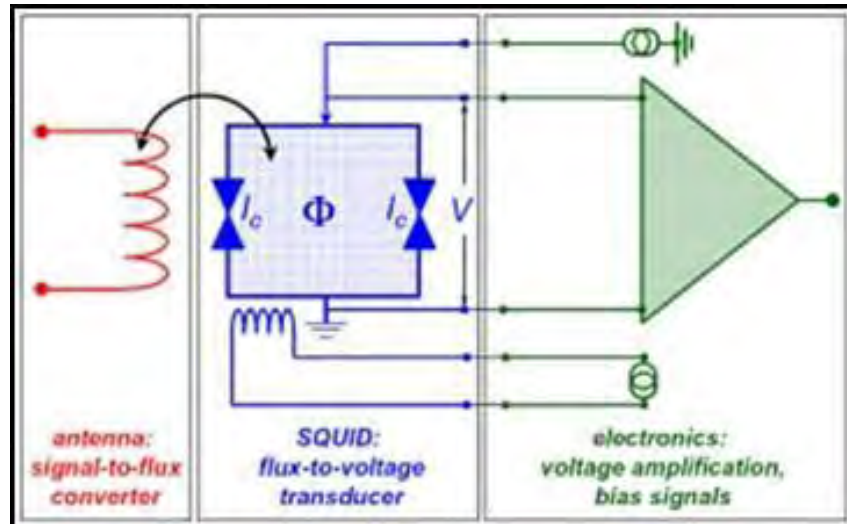
Figure 3.16: Schematic diagram of the working principle of SQUID magnetometer (flux to voltage converter).

To measure the magnetization of a sample, a field must be applied to the sample to induce a net moment in the sample. The net moment induced in the sample induces a current in the detector coils which are made from superconducting wire, the detector coils are connected to the SQUID and the output voltage of the SQUID is directly proportional to the current induced by the magnetization of the sample. Hence the SQUID acts as flux-to-voltage convertor (blue in figure 3.16). This voltage is then amplified and read out by the magnetometer's electronics (green in figure 3.16). In figure 3.17 the setup of the detection coils is shown.
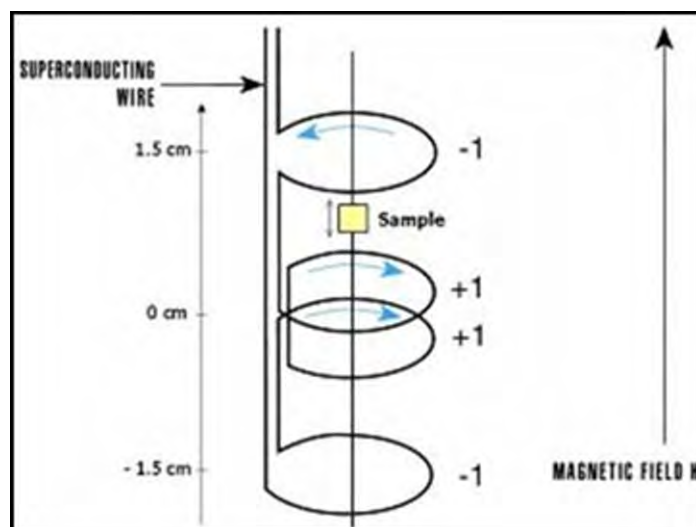
Figure 3.17: The detection coils of the SQUID magnetometer

There are coils at the top and bottom that are wound anti-clockwise and two central coils wound clockwise. This arrangement of detection coils means that variations of the magnetic field induce opposing current in the clockwise and anti-clockwise coils which cancel each other, thus minimizing noise in the detection circuit. The magnetization produced by the sample would not be uniform across the sample space, with the detection coils measuring the local changes in the magnetic flux density, in this way a current is induced in the detection coils by the sample's net magnetization. A cutaway view of the Quantum Design MPMS XL7 SQUID 45 magnetometer used for the measurement of magnetization of materials is shown in figure 3.18.
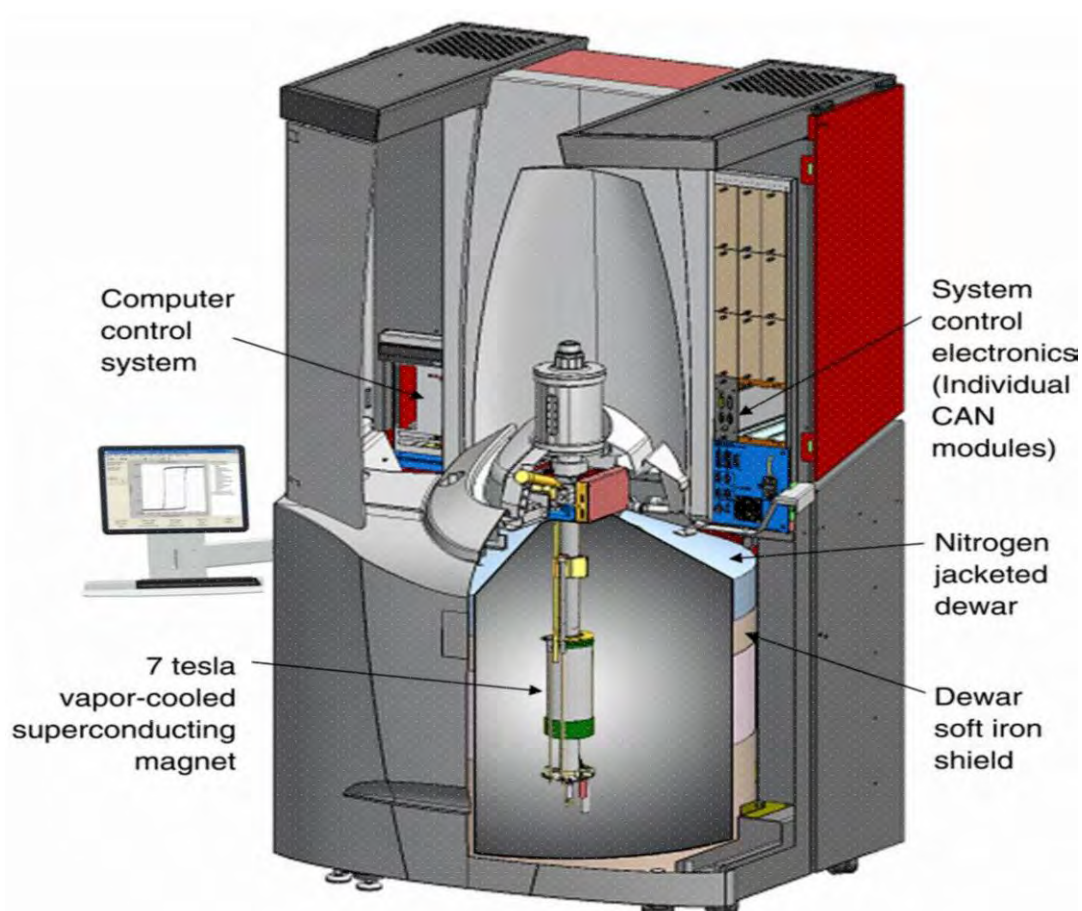
Figure 3.18: Cutaway view of the MPMS SQUID magnetometer

3.3.6 UV-vis spectrophotometer

The instrument used in ultraviolet-visible spectroscopy is called a UV-vis spectrophotometer. It uses light in the visible and adjacent (near-UV and near-infrared [NIR]) ranges. It measures the intensity of light passing through a sample (I), and compares it to the intensity of light before it passes through the sample (I_o). The ratio (I/I_o) is called the transmittance and is usually expressed as a percentage (%T). The absorbance (A) is based on the transmittance:

$$A= -\log (\%T/100) \tag{3.4}$$

The UV-visible spectrophotometer can also be configured to measure reflectance. In this case, the spectrophotometer measures the intensity of light reflected from a sample (I) and compares it to the intensity of light reflected from a reference material (I_o) (such as a white tile). The ratio (I/I_o) is called the reflectance, and is usually expressed as a percentage (%R).

The basic parts of a spectrophotometer are:

- ❖ a light source
- ❖ a holder for the sample
- ❖ a diffraction grating in a monochromator or a prism to separate the different wavelengths of light, and
- ❖ a detector

The radiation source is often a Tungsten filament (300-2500 nm), a deuterium arc lamp, which is continuous over the ultraviolet region (190-400 nm), Xenon arc lamp, which is continuous from 160-2,000 nm; or more recently, light emitting diodes (LED) [6] for the visible wavelengths. The detector is typically a photomultiplier tube, a photodiode, a photodiode array or a charge-coupled device (CCD). Single photodiode detectors and photomultiplier tubes are used with scanning monochromators, which filter the light so that only light of a single wavelength reaches the detector at one time. The scanning monochromator moves the diffraction grating to "step-through" each wavelength so that its intensity may be measured as a function of wavelength. Fixed monochromators are used with CCDs and photodiode arrays. As both of these devices consist of many detectors grouped into one or two

dimensional arrays, they are able to collect light of different wavelengths on different pixels or groups of pixels simultaneously.

A spectrophotometer can be either single beam or double beam. In a single beam instrument (such as the **Spectronic 20**), all of the light passes through the sample cell. I_o must be measured by removing the sample.

In a double-beam instrument, the light is split into two beams before it reaches the sample. One beam is used as the reference, the other beam passes through the sample. The reference beam intensity is taken as 100% Transmission (or 0 Absorbance), and the measurement displayed is the ratio of the two beam intensities.

Experimental set-up of a double-beam UV-vis spectrophotometer, (UV-2600, SHIMADZU) which was used for optical characterization of synthesized materials is shown (Figure 3.19).

Figure 3.19: UV-vis spectrophotometer, (UV-2600, SHIMADZU)

Samples for UV-vis spectrophotometry are most often liquids, although the absorbance of gases and even of solids can also be measured.

References:

[1] Cushing, B. L., Kolesnichenko, V. L., Connor, C. J. O., "Recent Advances in the Liquid-Phase Syntheses of Inorganic Nanoparticles", Chem. Rev., 104, 3893, 2004.

[2] Hasan, M., Islam, M. F., Mahbub, R., Hossain, M. S., Hakim, M. A., "A soft chemical route to the synthesis of $BiFeO_3$ nanoparticles with enhanced magnetization", Mat. Res. Bull., 73, 179, 2016.

[3] Das, S. C., Shahee, A., Lalla, N., P. and Shripathi, T. "A simple and low cost Sawyer-Tower ferro-electric loop tracer with variable frequency and compensation circuit", Proceedings of the 54th DAE Solid State Physics Symposium 54, 439, 2009.

[4] Rao, K. H., Raju, S. B., Aggarwal, K., Mendiratta, R. G., "Effect of Cr impurity on the dc resistivity of Mn-Zn ferrites", J. Appl. Phys., 52, 1376, 1981.

[5] Josephson, B. D., "The discovery of tunnelling supercurrents", Rev. Mod. Phys., 46, 251, 1974.

[6] Skoog, D. A., Holler, F. J., Crouch, S. R., "Principles of Instrumental Analysis (6th ed.)", Belmont, CA: Thomson Brooks/Cole, 169, 2007.

Chapter 4

Results and Discussion

The nominal composition of $BiFe_{1-x}Gd_xO_3$ (x = 0.00, 0.05) nanoparticles annealed at temperature ranging from 400 °C to 600 °C were synthesized by sol-gel method and their structural, electrical, dielectric, magnetic and optical properties were investigated. The outcomes of this investigation are described in this chapter.

4.1 Structural Characterizations

4.1.1. X-ray Diffraction

The structural properties of the synthesized nanoparticles was studied at room temperature (RT) by X-ray diffraction (XRD) using CuKα (λ=1.5418 Å) radiation. The X-ray diffraction patterns of $BiFe_{1-x}Gd_xO_3$ (x= 0.00, 0.05) nanoparticles annealed at temperature ranging from 400 °C to 600 °C are shown in figure 4.1.

All the XRD reflection peaks of pure $BiFeO_3$ are indexed and well matched with rhombohedral structure $R3c$ space group [1].

XRD patterns of $BiFe_{1-x}Gd_xO_3$ (x = 0.00, 0.05) nanoparticles annealed at temperature ranging from 400 °C to 600 °C reveled that some other peaks indicated by asterisk (*) in figure 4.1 have been observed and are attributed to secondary impurity phases [2]. These impurities are formed during synthesis of $BiFeO_3$. The low temperature stability of impurity phases and off-stoichiometric nature of $BiFeO_3$ are thought to be the prime causes for the formation of secondary phases [3-5].
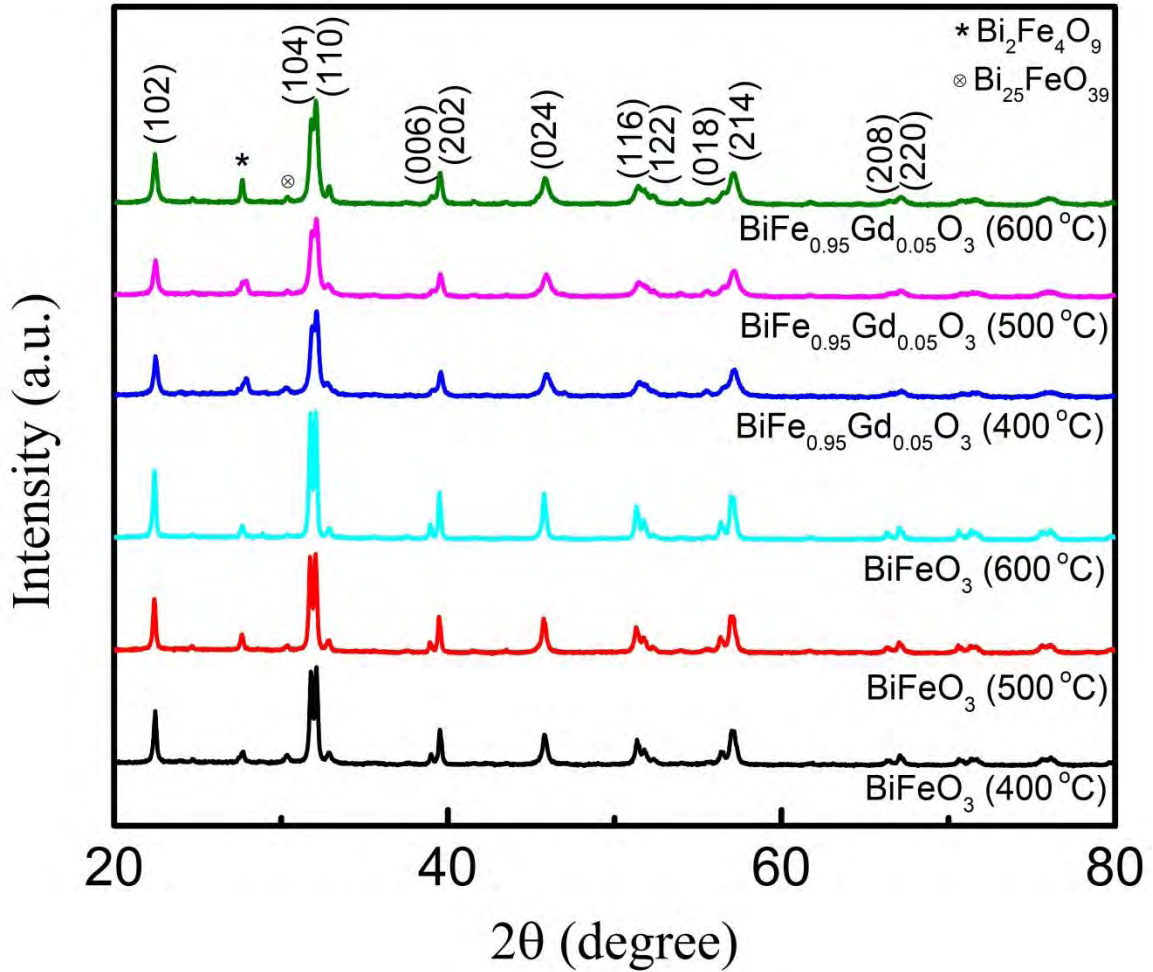
Figure 4.1: X-ray diffraction patterns of $BiFe_{1-x}Gd_xO_3$ (x= 0.00, 0.05) nanoparticles annealed at temperature ranging from 400 °C to 600 °C measured at RT.

The Miller indices (hkl) of the diffraction peaks in figure 4.1 are referred to hexagonal axes. The lattice parameters a and c of the hexagonal unit cell are calculated using the equation [6]:

$$\sin^2\theta = \frac{\lambda^2}{3a^2}(h^2 + hk + k^2) + \frac{\lambda^2 l^2}{4c^2}$$ (4.1)

where θ is Bragg"s angle. The strong peaks (102) and (110) were employed for such calculations. The calculated values of lattice parameters (equivalent to hexagonal) of $BiFe_{1-x}Gd_xO_3$ (x=0.00, 0.05) nanoparticles annealed at temperature ranging from 400 °C to 600 °C shown in table 1:

Table: 1

The table shows the calculated lattice parameters of the synthesized nanoparticles

Annealing temperature (°C)	Sample	Lattice parameters		Sample	Lattice parameters	
		a = b (Å)	c (Å)		a = b (Å)	c (Å)
400	$BiFeO_3$	5.568	13.832	$BiFe_{0.95}Gd_{0.05}O_3$	5.563	13.801
500	$BiFeO_3$	5.573	13.863	$BiFe_{0.95}Gd_{0.05}O_3$	5.568	13.804
600	$BiFeO_3$	5.575	13.864	$BiFe_{0.95}Gd_{0.05}O_3$	5.573	13.806

The calculated of lattice parameters matched well with previous literatures [7, 8], and indicates a continual change in lattice constant when Gd^{3+} ion is substituted for Fe^{3+} ion and annealing temperature was changed. For undoped $BiFeO_3$ the lattice constants a and c are increased with annealing temperature. However for Gd doped $BiFeO_3$ the a and c lattice constants decreases with the increase of temperature.

To further investigate the influence of Gd doping, a magnified view of the XRD patterns, in the vicinity of 2θ around 32 degrees has been shown in figure 4.2. It is observed that the twin Bragg-peak [(104) and (110)] tends to merge into a single diffraction peak in $BiFe_{0.95}Gd_{0.05}O_3$ due to the difference in the ionic radii of Gd^{3+} (0.938 Å) and Fe^{3+} (0.645 Å) [9].
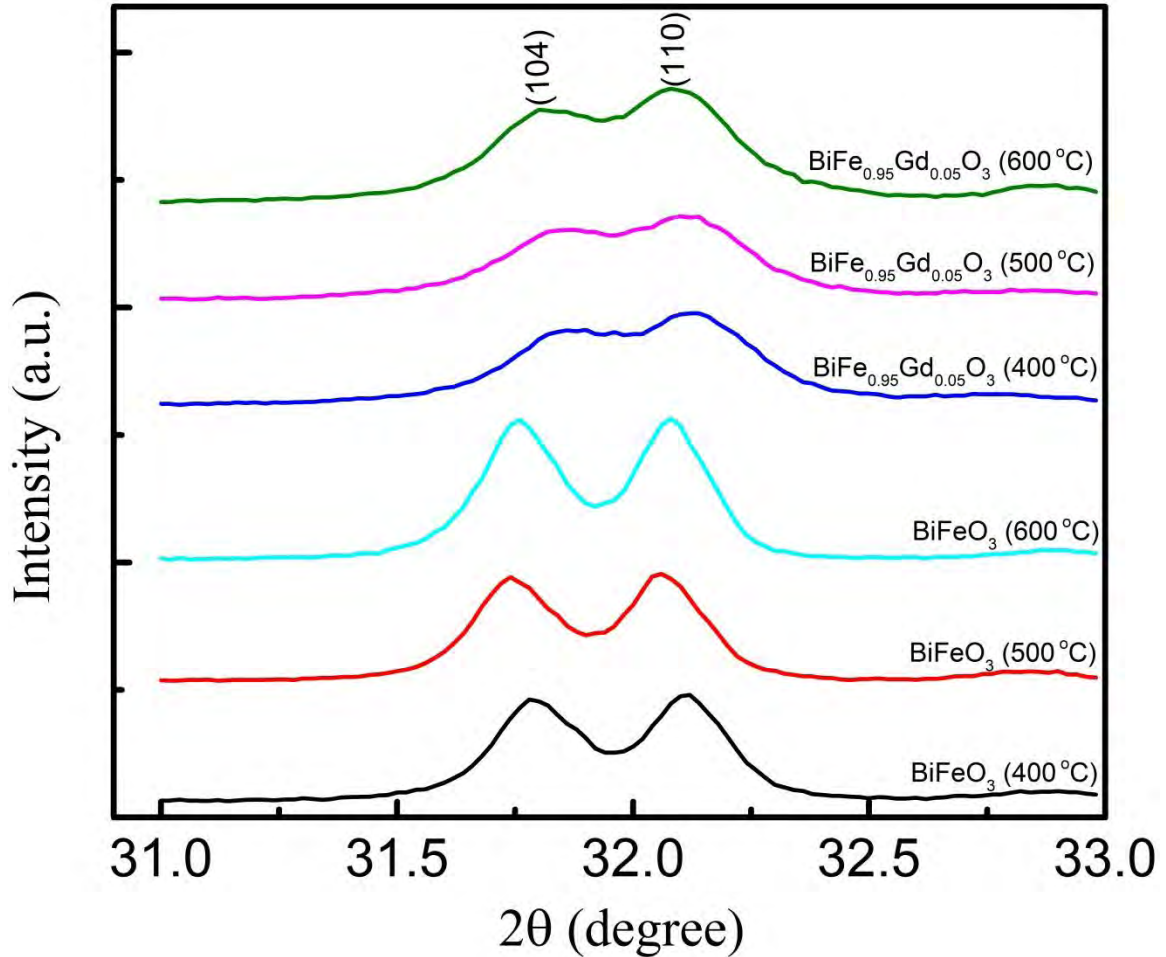
Figure 4.2: Magnified XRD patterns of (104) and (110) reflections at $2\theta = 32°$ for of $BiFe_{1-x}Gd_xO_3$ (x= 0.00, 0.05) nanoparticles annealed at temperature ranging from 400 °C to 600 °C.

The decrease in the splitting of (104) and (110) peaks in $BiFe_{0.95}Gd_{0.05}O_3$ nanoparticles around $2\theta = 32°$ together with the changing lattice parameters indicates that the rhombohedral $BiFeO_3$ structure has a tendency to change rhombohedral to orthorhombic crystal structure [10].

Previous investigation demonstrates that for a higher amount of Gd content (x $\geq$ 0.10) in host $BiFeO_3$ nanoparticles, the splitting of (104) and (110) reflection peaks was completely removed and merged into one broad peak [10]. That result suggests that doping of 5% Gd in $BiFeO_3$ can avoid a complete structural transformation from rhombohedral to orthorhombic [10, 11].

The average crystallite size (d) was calculated from XRD patterns by applying Scherrer formula [2]:

$$d = \frac{k\lambda}{\beta cos\theta}$$ (4.2)

where k is the dimensionless shape factor with a typical value of about 0.94, λ is the wavelength of CuKα radiation with the value of 1.5418 Å, θ is the Bragg angle for the (102) diffraction peak and β is the full width at half maximum (FWHM) intensity of the corresponding diffraction peak.

Crystallite size calculated using Scherrer formula are presented in table 2:

Table: 2

The table shows the average crystallite size (calculated from XRD patterns) and average particle size (calculated from FESEM images)

Annealing temperature (°C)	From XRD patterns				From FESEM images			
	Sample	Average crystallite size (nm)	Sample	Average crystallite size (nm)	Sample	Average particle size (nm)	Sample	Average particle size (nm)
400	BFO	41	BFGO	32	BFO	57	BFGO	57
500	BFO	44	BFGO	31	BFO	75	BFGO	46
600	BFO	44	BFGO	31	BFO	124	BFGO	35

From table it is seen that due to the substitution of Gd the crystallite size was found to reduce. However, the annealing temperature increased the crystallite size was found to increase in the case of undoped $BiFeO_3$. From table it is also observed that the average particle size obtained from FESEM images is larger than that calculated from the XRD patterns using Scherrer equation. Due to the high degree of agglomeration of the particles

as was seen in FESEM image, it was really difficult to estimate the particle size. Similar large deviation in particle size determined by FESEM images and that calculated by Scherrer equation has also been reported in previous investigations [12, 13] and was attributed to the agglomeration of the particles.

4.2 Investigation of particle size distribution

To estimate the particle size distribution of $BiFe_{1-x}Gd_xO_3$ (x=0.00, 0.05) nanoparticles annealed at temperature ranging from 400 °C to 600 °C, field emission scanning electron microscopy (FESEM) images were taken. The FESEM images of all compositions and their corresponding particle size distribution are shown in figure 4.3.

FESEM image of figure 4.3 (a), (b) and (c) and their corresponding histograms shows that the average particle size of undoped $BiFeO_3$ (BFO) sample, annealed at 400 °C, 500 °C and 600 °C are ranging from 30 nm to 80 nm, 40 nm to 100 nm and 80 nm to 140 nm respectively. From figure 4.3 (d), (e) and (f) and their corresponding histograms shows the average particle size of 5% Gd doped $BiFeO_3$ (BFGO) sample, annealed at 400 °C, 500 °C and 600 °C are ranging from 20 nm to 80 nm, 20 nm to 60 nm and 20 nm to 50 nm respectively.
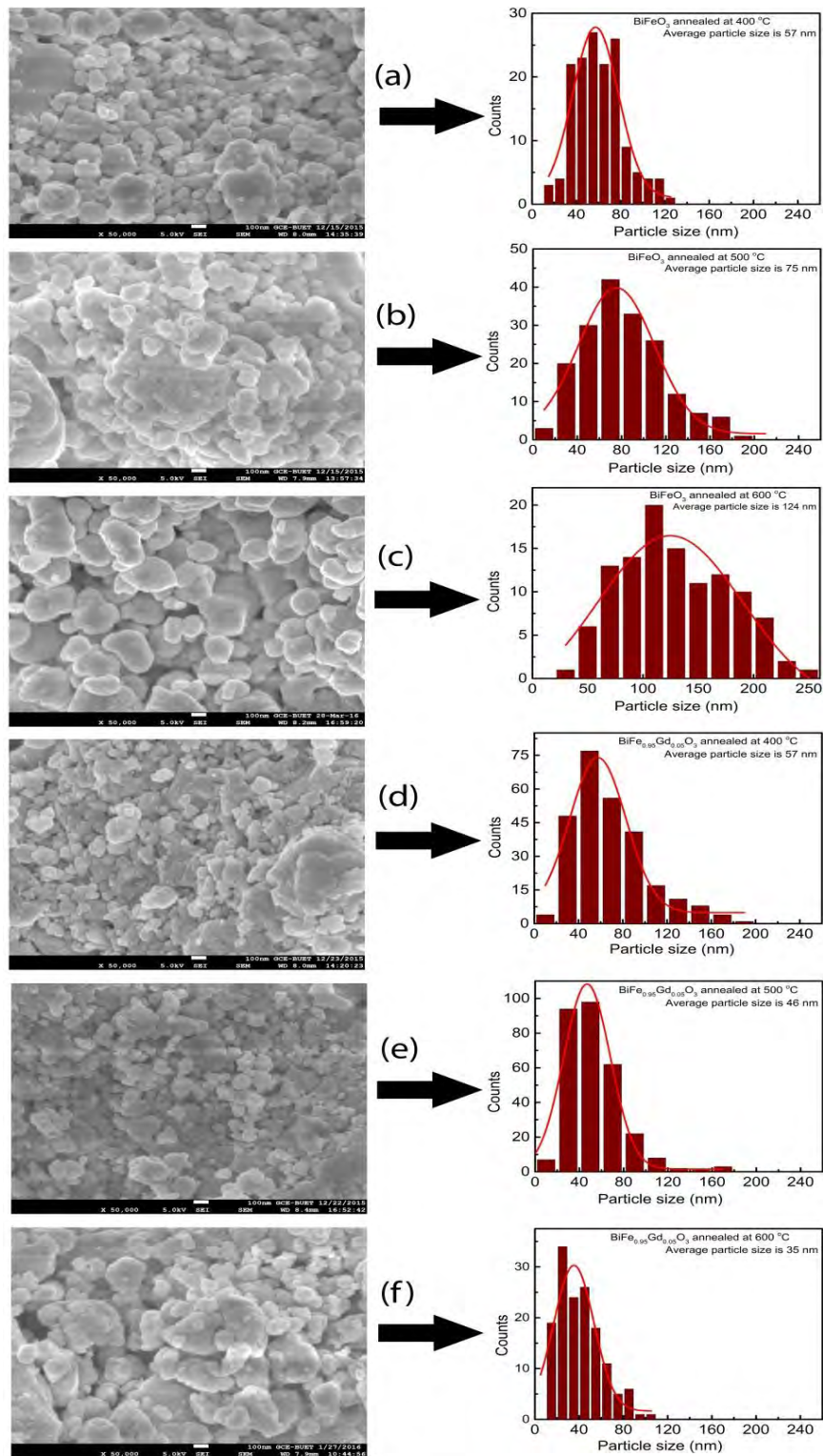
Figure 4.3: FESEM imaging BiFe$_{1-x}$Gd$_x$O$_3$ nanoparticles: (a) x = 0.00 (400 °C), (b) x = 0.00 (500 °C), (c) x = 0.00 (600 °C), (d) x = 0.05 (400 °C), (e) x = 0.05 (500 °C), (f) x = 0.05 (600 °C) and their respective histograms.

We can see from this investigation that, the average particle size of pure $BiFeO_3$ is increasing with annealing temperature, however, the particle size of 5% Gd doped $BiFeO_3$ is decreasing. Notably at higher annealing temperature it seems some agglomeration occur in case of 5% Gd doped $BiFeO_3$. The increase of average particle size of pure $BiFeO_3$ and decrease of average particle size of 5% Gd doped $BiFeO_3$ with increasing annealing temperature is consistent with average crystallite size that calculated from XRD result (shown in table 2).

The average particle size in the 5% Gd doped $BiFeO_3$ samples were significantly reduced probably due to the suppression of the formation of oxygen vacancies. It is expected that the decreased oxygen vacancies helps in densification and lead to a lower grain growth [14]. To justify this statement we have carried out leakage current density measurements and the result will be presented in the next section.

4.3 Ferroelectric (P-E) measurements

The polarization vs electric field (P-E) hysteresis loops measured at a frequency of 50 Hz at room temperature has been carried out to study the effect of Gd doping on the ferroelectric properties of $BiFeO_3$ (BFO) nanoparticles. First of all, to examine the leaky behavior of $BiFeO_3$ (BFO) nanoparticles and $BiFe_{0.95}Gd_{0.05}O_3$ (BFGO) nanoparticles, leakage current density, J versus electric field, E measurements were performed for an applied field 10 kV/cm.

Figure 4.4 revealed the effect of Gd-doping and particle size on leakage current density of $BiFeO_3$ nanoparticles. The high leakage current of undoped $BiFeO_3$ in this study may be connected with impurity phases, oxygen vacancies and electron hopping from Fe^{2+} to Fe^{3+} state [15, 16].
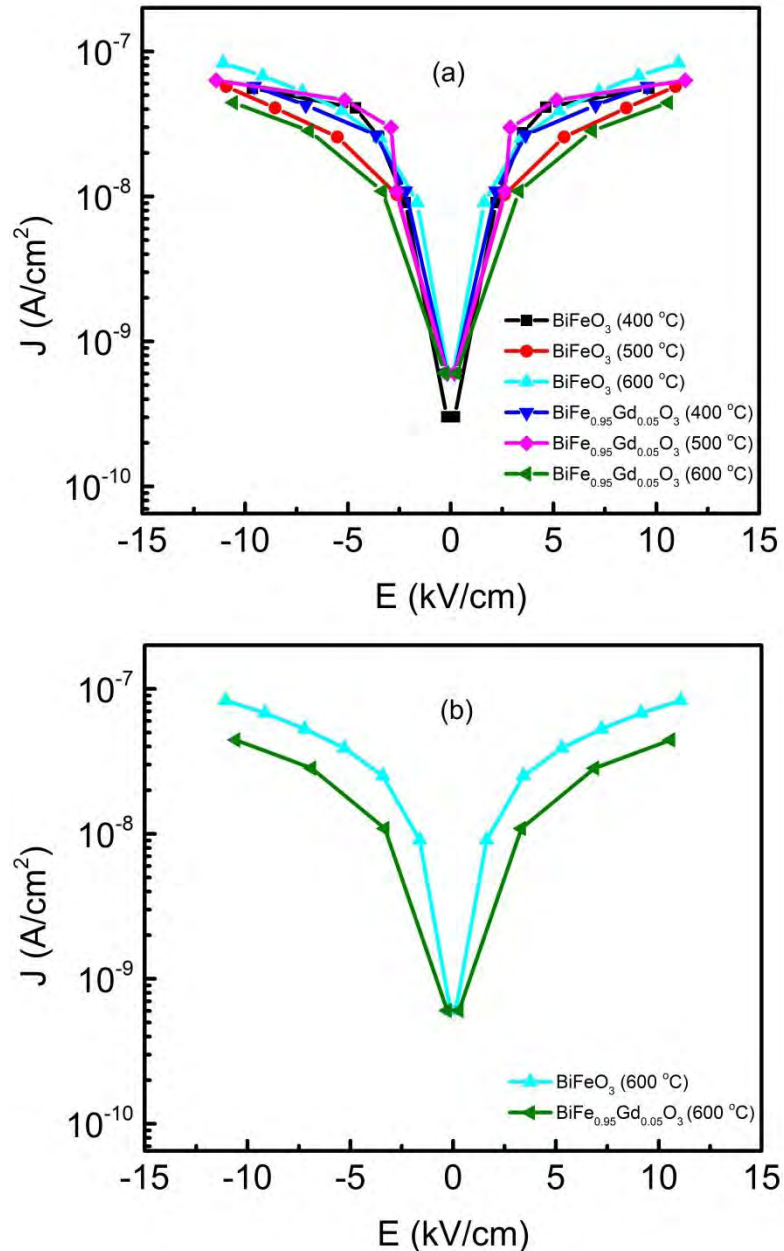
Figure 4.4: (a) Room temperature leakage current density, J versus applied field, E plot for BFO and BFGO nanoparticles annealed at different temperatures, (b) Figure shows separately the leakage current difference between pure BFO and BFGO annealed at 600 $^{\circ}$C.

Mixed valency of Fe and the formation of oxygen vacancy provide free charge carriers to enhance leakage current [17]. Due to the substitution of Gd in BFO the leakage current density was found to decrease. When considering the effect of Gd doping and annealing temperature on leakage current density, it is clear from figure 4.4 that in case of 5% Gd-

doped $BiFeO_3$ nanoparticles annealed at 600 °C the leakage current density reduced by a considerable amount. It is also observed from FESEM imaging that the particle size of 5% Gd-doped in $BiFeO_3$ nanoparticles annealed at 600 °C was also smallest.

Table: 3

The table shows the leakage current density of BFO and BFGO nanoparticles annealed at temperature ranging from 400 °C to 600 °C.

Applied field	Annealing temperature (°C)	Sample	Particle size (nm)	Leakage current density (J) (A/cm^2)	Sample	Particle size (nm)	Leakage current density (J) (A/cm^2)
10 kV	400	BFO	57	5.56×10^{-8}	BFGO	57	5.74×10^{-8}
	500	BFO	75	5.74×10^{-8}	BFGO	46	6.41×10^{-8}
	600	BFO	124	8.25×10^{-8}	BFGO	35	4.47×10^{-8}

From table we can see that, for pure BFO both the leakage current and particle size increases with the annealing temperature whereas the leakage current density and particle size decreases for BFGO.

Therefore, the replacement of smaller Fe^{3+} (0.645Å) by larger Gd^{3+} (0.938 Å) ion is supposed to hinder ion mobility and thereby may also reduce leakage current [16].

We have also carried out ferroelectric measurement to establish polarization versus electric field hysteresis loops (P-E) at an applied field ±10 kV/cm for BFO and BFGO nanoparticles. The P-E loops of BFO and BFGO nanoparticles annealed at temperature ranging from 400 °C to 600 °C are shown in figure 4.5 which actually demonstrates the effect of Gd-doping and particle size variation. The ferroelectricity of all synthesized nanoparticles was evidenced by the P-E loops.
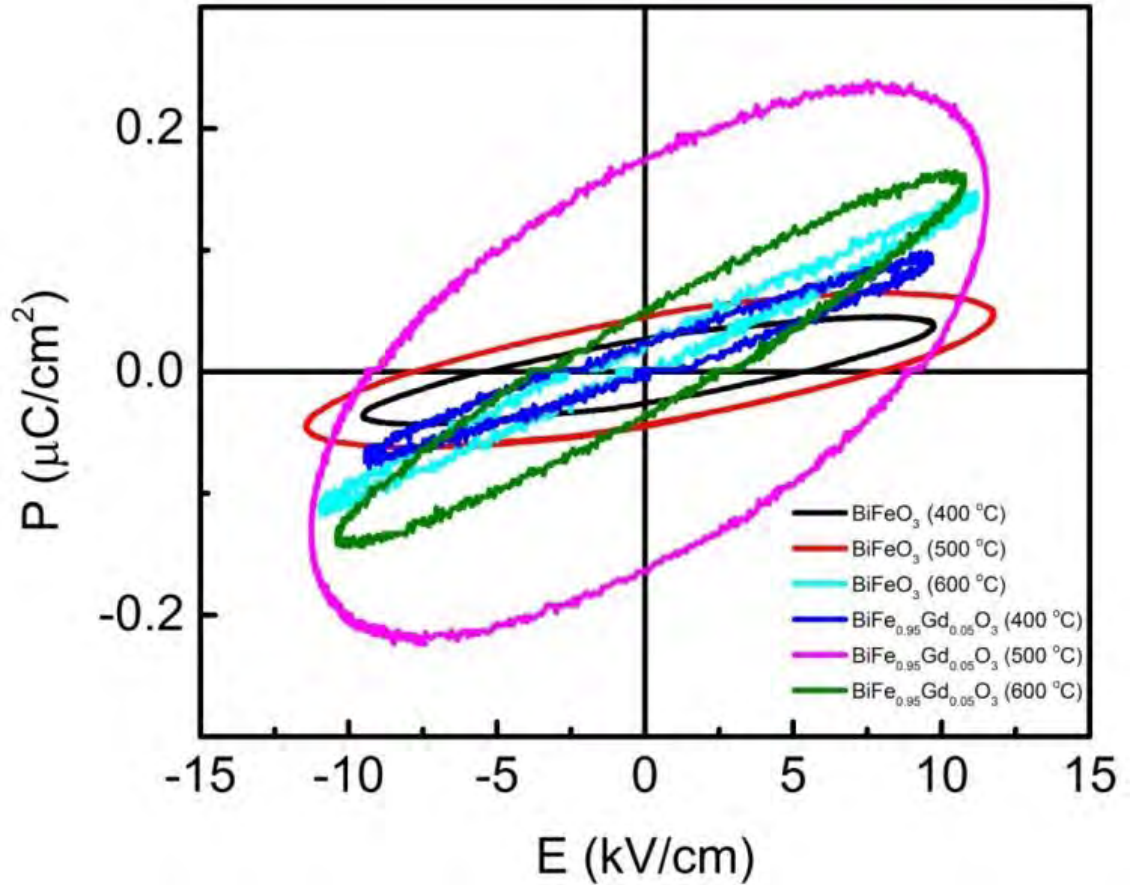
Figure 4.5: The room temperature P-E hysteresis loops of $BiFe_{1-x}Gd_xO_3$ (x = 0.00, 0.05) nanoparticles annealed at temperature ranging from 400 °C to 600 °C measured at applied field 10 kV/cm.

From figure we can see that at low applied field the $BiFe_{0.95}Gd_{0.05}O_3$ nanoparticles annealed at 500 °C shows maximum remanent polarization (P_r = 0.1709 $\mu C/cm^2$) compared to others (shown in table 4), but the shape of P-E loop is less elliptical which is occurred due to the high leakage current density (figure 4.4(a)). In the case of the $BiFe_{0.95}Gd_{0.05}O_3$ nanoparticles annealed at 600 °C, (figure 4.5), having the smallest particle size (35 nm), the P-E loop become more and more typical than other compositions which is expected due to their reduced leakage current density (figure 4.4(a)) [18].

Table: 4

The table shows the calculated values of Remnant Polarization (P_r) and Coercive field (E_c) of BFO and BFGO nanoparticles measured at room temperature.

Applied field	Annealing temperature (°C)	Sample	Particle size (nm)	Remnant Polarization (P_r) ($\mu C/cm^2$)	Coercive field (E_c) (kV/cm)	Sample	Particle size (nm)	Remnant Polarization (P_r) ($\mu C/cm^2$)	Coercive field (E_c) (kV/cm)
10 kV	400	BFO	57	0.0265	5.46	BFGO	57	0.0147	1.70
	500	BFO	75	0.0442	7.88	BFGO	46	0.1709	9.10
	600	BFO	124	0.0102	1.13	BFGO	35	0.0453	3.18

The cause of this result is that, when Gd^{3+} substitutes Fe^{3+}, there is no acceptor doping of Fe^{3+} by Fe^{2+}, and hence this cannot cause a decrease in the conductivity. Here structural distortion plays a role in improving the ferroelectricity in Gd^{3+} doped $BiFeO_3$. Gd^{3+} ions occupy the Fe site and lies in the oxygen octahedron to form Gd^{3+} 3d-O 2p hybridization. Since the bond dissociation energy of the Gd–O bond (719 ± 6 kJ/mol) is stronger than that of the Fe–O bond (407 ± 1kJ/mol) [19] the substitution of isovalent Gd^{3+} ions at the Fe site of BFO will reduce the oxygen vacancies generated by Fe ions. This leads to improved ferroelectric properties due to enhanced stabilization of the ferroelectric distortion.

Therefore, due to low leakage current and most typical ferroelectric behavior the $BiFe_{0.95}Gd_{0.05}O_3$ nanoparticles annealed at 600 °C might have potential technological applications.

4.4 Dielectric Measurements

Figure 4.6 illustrates the frequency dependence of the dielectric constant (ε') of $BiFe_{1-x}Gd_xO_3$ (x = 0.00, 0.05) nanoparticles annealed at temperature ranging from 400 °C to 600 °C measured at room temperature in the frequency range 100 Hz–10MHz.
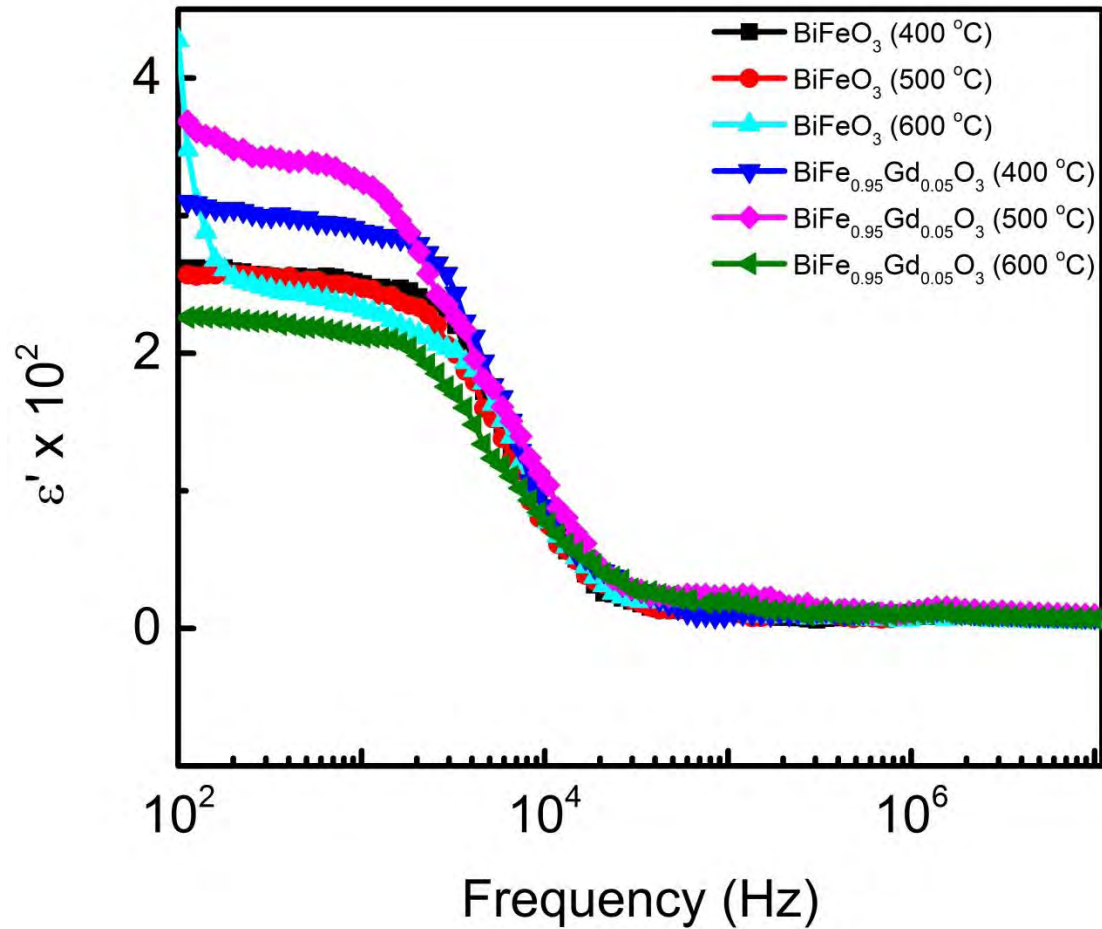
Figure 4.6: Semi-log plot of dielectric constant as a function of frequency of $BiFe_{1-x}Gd_xO_3$ (x = 0.00, 0.05) nanoparticles annealed at temperature ranging from 400 °C to 600 °C measured at RT.

It can be seen from figure that, the dielectric constant for all the synthesized nanoparticles is maximum at lower frequencies which decreases sharply with increasing frequency up to about 25 kHz and shows nearly frequency independent behavior at higher frequencies

>25 kHz (shown in table 5), which is consistent with a combined response of orientational relaxation of dipoles and conduction of charge carriers [20].

Table: 5

The table shows the dielectric constant of $BiFeO_3$ (BFO) and $BiFe_{0.95}Gd_{0.05}O_3$ (BFGO) nanoparticles measured at room temperature.

Frequency (Hz)	Dielectric constant of the synthesized nanoparticles					
	BFO (400 °C)	BFGO (400 °C)	BFO (500 °C)	BFGO (500 °C)	BFO (600 °C)	BFGO (600 °C)
500	255	297	253	339	243	218
1500	246	284	240	302	223	208
5000	164	183	156	177	168	126
10×10^3	82	98	76	107	81	78
2.5×10^4	25	35	29	33	22	36
2×10^5	8	12	10	18	10	13
6×10^6	8	8	8	10	6	7

Form table it is seen that, at low frequency the dielectric constant is highest for 5% Gd doped BFO nanoparticles which annealed at 500 °C. Notably, high values of dielectric constant at low frequency are not intrinsic properties of the samples, but they are rather associated with charge defects as well as their reaction features to the driven frequency [21].

This low frequency dispersion is common in dielectric and ferroelectric (Example: $BiFeO_3$) materials due to the finite conductivity arising from oxygen vacancies [22, 23] and space charge or interfacial polarization as discussed by Maxwell [24] and Wagner [25]. Four types of polarization: (a) electronic (b) atomic or ionic (c) dipolar and (d) interfacial or space charge polarization, contribute to total polarization. Dipolar polarization contributes in the sub-infrared frequency range (10^3 - 10^6 Hz) [26]. It is impossible for dipolar polarization to follow the electric field in the microwave region, whereas interfacial or space charge polarization contributes only in the lower frequency range (~ 10^3 Hz). At low frequencies, the space charges are able to follow the frequency

of the applied field, while at a high frequency they may not have time to build up and undergo relaxation. Therefore at higher frequencies ε' is smaller as all polarization do not contribute at high frequencies.

From figure 4.6 it is seen that, at lower frequency the dielectric constant is lower for $BiFe_{0.95}Gd_{0.05}O_3$ nanoparticles annealed at temperature 600 $^{\circ}$C. From the electric measurements it is found that the leakage current density is smallest for this sample. The phenomenon of oxygen vacancies has direct correspondence with the leakage current density [27]. So, for lowest dielectric constant and leakage current density we can say that $BiFe_{0.95}Gd_{0.05}O_3$ nanoparticles annealed at 600 °C has low concentration of charge defects such as oxygen vacancies [27].

The dielectric loss tangent also shows frequency dependency as illustrated in figure 4.7.

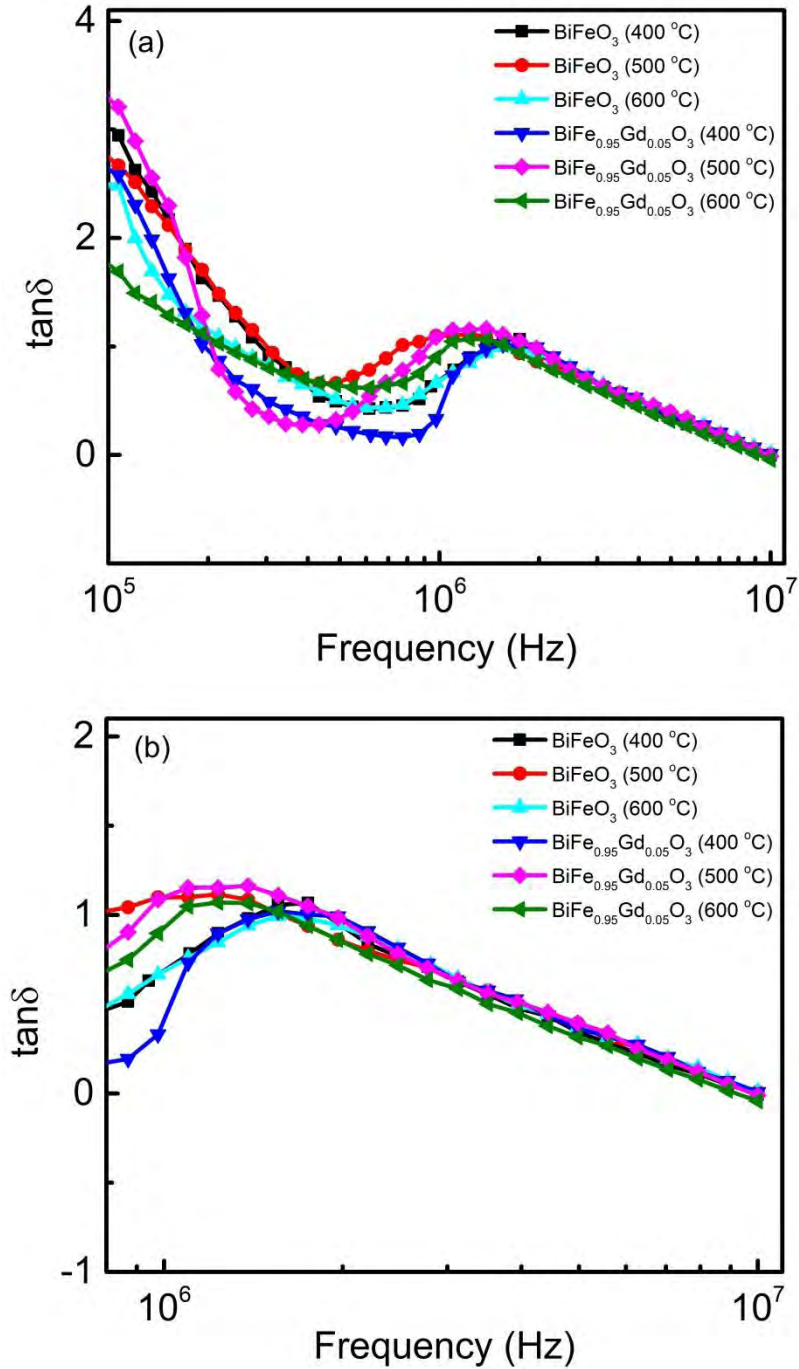**Figure 4.7:** (a) Variation in frequency dependence of tangent loss (tan δ) and (b) Magnified view of variation in frequency dependence of tangent loss (tan δ) of $BiFe_{1-x}Gd_xO_3$ (x = 0.00, 0.05) nanoparticles annealed at temperature ranging from 400 °C to 600 °C measured at RT.

The dielectric loss tangent for all the samples decreasing gradually with the increase of frequency (shown in table 6). At the frequency 100 kHz the dielectric loss is lower for $BiFe_{0.95}Gd_{0.05}O_3$ nanoparticles annealed at 600 °C compared with other samples.

Table: 6

The table shows the dielectric loss tangent of BFO and BFGO nanoparticles annealed at temperature ranging from 400 °C to 600 °C

Frequency (Hz)	Dielectric loss tangent of BFO and BFGO nanoparticles					
	BFO (400 °C)	BFGO (400 °C)	BFO (500 °C)	BFGO (500 °C)	BFO (600 °C)	BFGO (600 °C)
1×10^5	3.016	2.621	2.743	3.268	2.489	1.752
2×10^5	1.575	0.973	1.633	1.089	1.167	1.089
4×10^5	0.626	0.315	0.684	0.276	0.626	0.684
1×10^6	0.715	0.424	1.104	1.104	0.715	0.949
1.5×10^6	1.050	1.031	1.031	1.128	0.973	1.031
3.5×10^6	0.543	0.557	0.557	0.556	0.576	0.505
1×10^7	0.042	0.042	0.042	0.023	0.042	0.004

From table it is also visible that the dielectric loss tangent is lower for $BiFe_{0.95}Gd_{0.05}O_3$ nanoparticles annealed at 600 °C at higher frequencies. This nanoparticles also have lower leakage current (figure 4.4 (a)). Due to lower leakage current and lower dielectric loss tangent at higher frequencies the $BiFe_{0.95}Gd_{0.05}O_3$ nanoparticles annealed at 600 °C might have potential applications in high-frequency microwave devices [5].

It can be seen by comparing figures 4.6 and 4.5 that the dielectric constant and remnant polarization follow exactly the same trend. This similarity is hardly surprising because polarization is related to electric field through the dielectric constant. The larger is the dielectric constant, the easier is the aligning up of the dipoles along the poling field and consequently the larger is the remnant polarization (P_r). In general, the remnant polarization of a ferroelectric is proportional to the dielectric constant [21]. It should be

emphasized that the dielectric constant in figure 4.6 and the remnant polarization in figure 4.5 were obtained independently using different experimental techniques. The revealed relationship between them indicates that our data are reliable and the dielectric behaviour found in this work is an intrinsic feature of these Gd doped BFO nanoparticles, rather than an experimental artifact.

4.5 Magnetic Characterization

For magnetic characterization of the synthesized nanoparticles magnetization versus applied magnetic field (M-H) hysteresis loops were carried out at room temperature (RT) using SQUID magnetometer. M-H curves for $BiFeO_3$ (BFO) and $BiFe_{0.95}Gd_{0.05}O_3$ (BFGO) nanoparticles annealed at temperatures ranging from 400 °C to 600 °C measured at RT with an applied magnetic field of up to ±20 kOe are shown in figure 4.8.
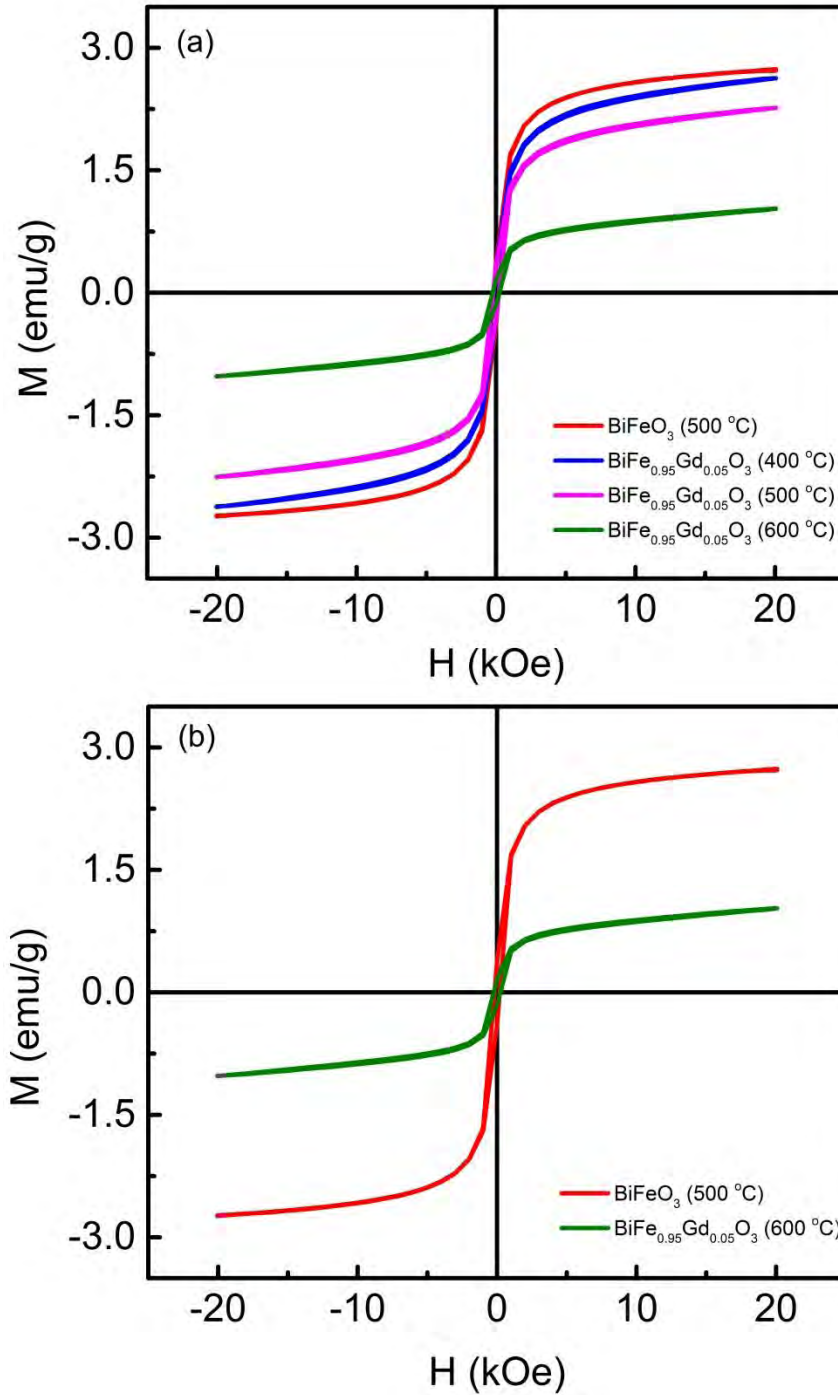
Figure 4.8: (a) M-H hysteresis curves of $BiFeO_3$ and $BiFe_{0.95}Gd_{0.05}O_3$ nanoparticles measured at RT, (b) Highest and lowest saturation magnetization graph of $BiFeO_3$ and $BFe_{0.95}Gd_{0.05}O_3$ nanoparticles.

Figure 4.8 indicating the saturation magnetization (M_s) achieved in all the samples within the applied field of ±20 kOe. The observed hysteresis loop is a confirmation of the presence of ferromagnetic interaction in the samples. Figure 4.9 demonstrate the Arrot-Belov-Kouvel (ABK) plot of the synthesized nanoparticles [28].
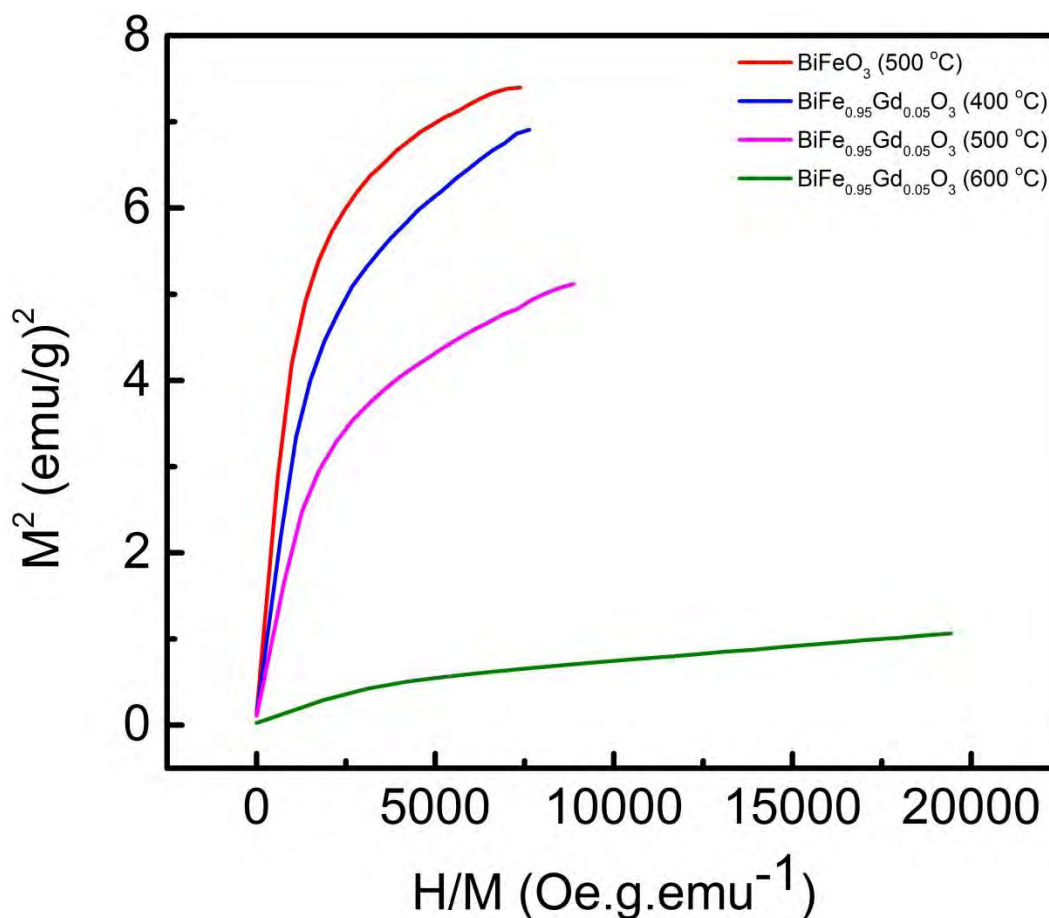
Figure 4.9: ABK plot in order to determine saturation magnetization of the synthesized nanoparticles.

ABK plot also signifies the presence of ferromagnetic interaction in a system and measures the saturation magnetization in the samples [29]. In the ABK plot, M^2 is plotted against H/M and the saturation magnetization is measured from the intercept of the linear fitting of the curve on Y-axis. The saturation magnetization of $BiFeO_3$ (500 ^{o}C), $BiFe_{0.95}Gd_{0.05}O_3$ (400 ^{o}C), $BiFe_{0.95}Gd_{0.05}O_3$ (500 ^{o}C) and $BiFe_{0.95}Gd_{0.05}O_3$ (600 ^{o}C) nanoparticles are 2.23 emu/g, 2.00 emu/g, 1.66 emu/g, 0.57 emu/g respectively.

The saturation magnetization is highest for pure $BiFeO_3$ nanoparticles and gradually decreasing for Gd doped $BiFeO_3$ nanoparticles with increasing annealing temperature, but the values of M_s of all synthesized nanoparticles has been found to be significantly higher than that of bulk $BiFeO_3$ ($M_s \sim 0.005$ emu/g) [11].

It is well known that undoped $BiFeO_3$ bulk ceramic is an antiferromagnetic below $T_N \sim$ 643 K [14]. However, the sol-gel derived undoped $BiFeO_3$ nanoparticles exhibit a ferromagnetic nature. It is reported that the contribution of uncompensated spins at the particle surface increases sharply with decreasing particle size [30] and may subscribe to this enhanced magnetization in $BiFeO_3$ nanoparticles.

The onset of ferromagnetism in Gd doped $BiFeO_3$ nanostructures could be attributed to the suppression of spiral spin order and structural distortion by Gd-doping which is quantified as changes in Fe-O-Fe bond angle. The change in bond angle modifies the tilting angle of FeO_6 octahedron which might suppress the spiral spin structure and hence outset net magnetization in $BiFe_{0.95}Gd_{0.05}O_3$ nanoparticles. As reported previously, Gd doped at Fe site of $BiFeO_3$ shows a lower magnetization value [31, 32]. The substitution of Fe^{3+} (0.63 Å) by dopant with higher ionic radius (0.93 Å) distorts the lattice structure and reduce magnetization.

Notably, the unseen defects in the undoped $BiFeO_3$ nanoparticles may also cause enhanced magnetization. Therefore, decrease in the saturation magnetization of Gd doped $BiFeO_3$ indicates weakening of the ferromagnetic interaction with the reduction in defect content, mostly oxygen vacancies in the synthesized nanoparticles [28].

Figures 4.10 (a)–4.10 (d) demonstrate an enlarged view of the low-field M-H hysteresis loops of $BiFe_{1-x}Gd_xO_3$ nanoparticles; (a) x =0.00 (500 °C), (b) x = 0.05 (400°C), (c) x = 0.05 (500 °C), (d) x = 0.05 (600 °C) measured at RT. From figures 4.10 (a)–4.10 (d), a non-zero remanent magnetization and coercive field are observed for all the samples. The remanent magnetization (M_r) is defined as $M_r = |(M_{r1} − M_{r2})| / 2$, where M_{r1} and M_{r2} are the magnetization with positive and negative points of intersection with H = 0, respectively [33]. The coercive field (H_c) is given by $H_c = |(H_{c1} − H_{c2})|/2$, where H_{c1} and

H_{c2} are the left and right coercive fields [33] respectively. The calculated values of M_r and H_c were summarized in table: 7.
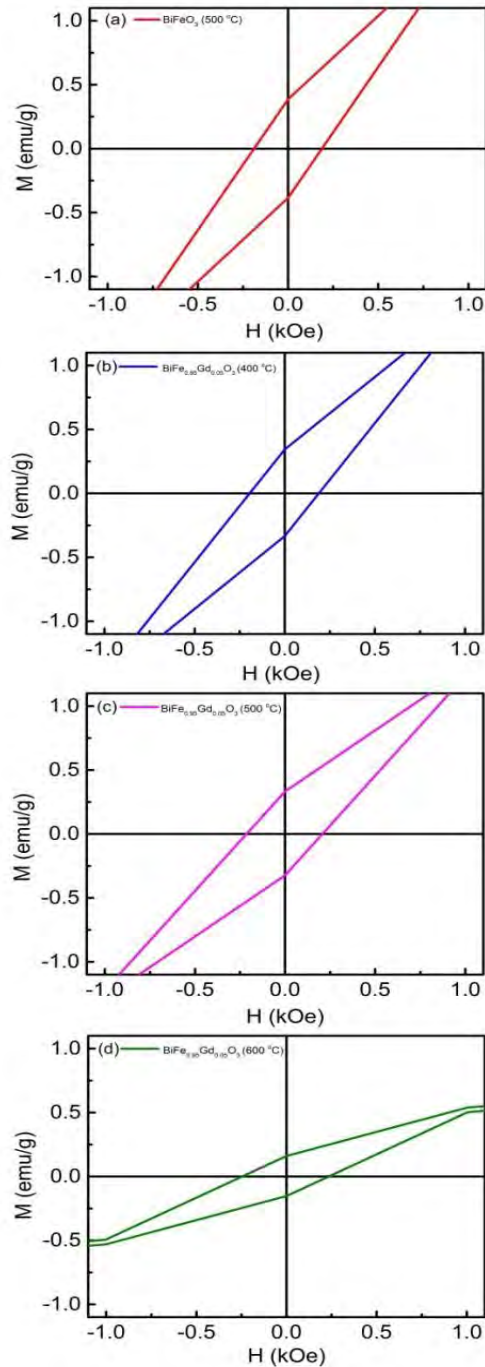

Figure 4.10: An enlarged view of the low-field M-H hysteresis loop of BiFe$_{1-x}$Gd$_x$O$_3$ nanoparticles; (a) x =0.00 (500 °C), (b) x = 0.05 (400°C), (c) x = 0.05 (500 °C), (d) x = 0.05 (600 °C).

Table: 7

The table shows the calculated values of saturation magnetization (M_s) remanent magnetization (M_r) and coercive field (H_c)

Annealing temperature (°C)	Sample	Particle size (nm)	Remanent magnet- ization (M_r) emu/g	Coercive field (H_c) kOe	Sample	Particle size (nm)	Remanent magnet- ization (M_r) emu/g	Coercive field (H_c) kOe
500					BFGO	57	0.34	0.19
400	BFO	75	0.39	0.19	BFGO	46	0.33	0.21
500					BFGO	35	0.15	0.24

From the table it is found that, the remanent magnetization (M_r) was gradually decreasing and coercive filed (H_c) gradually increasing with decreasing particle size and increasing annealing temperature [26]. The table reveals that 35nm $BiFe_{0.95}Gd_{0.05}O_3$ nanoparticles show highest H_c (0.24 kOe) although show lowest M_r (0.15 emu/g). Such high coercivity may be caused by the magnetic anisotropy [26]. The observed H_c value for 35nm $BiFe_{0.95}Gd_{0.05}O_3$ nanoparticles is in good agreement with some previously published values [34].

4.6 Optical Characterization

The UV-visible diffuse reflectance spectra (DRS) of the synthesized nanoparticles were investigated with an aim to investigate their optical properties. The UV-visible diffuse reflectance spectra of $BiFe_{1-x}Gd_xO_3$ (x = 0.00, 0.05) nanoparticles annealed at temperature ranging from 400 °C to 600 °C are shown in figure 4.11: (a), (b), (c), (d), (e) and (f) respectively. The band gap energy of these nanoparticles were estimated from their UV-visible diffuse reflectance spectra by applying Kubelka-Munk (KM) function given by $F(R) = \frac{(1-R)^2}{2R}$, where R is the reflectance value [35]. Figure 4.11: (g), (h), (i), (j), (k) and (l) shows the $[F(R)*hv]^{1/2}$ vs. hv plots for the synthesized samples where the tangent line with $[F(R)*hv]^{1/2} = 0$ is the band gap energy of the corresponding material [35].
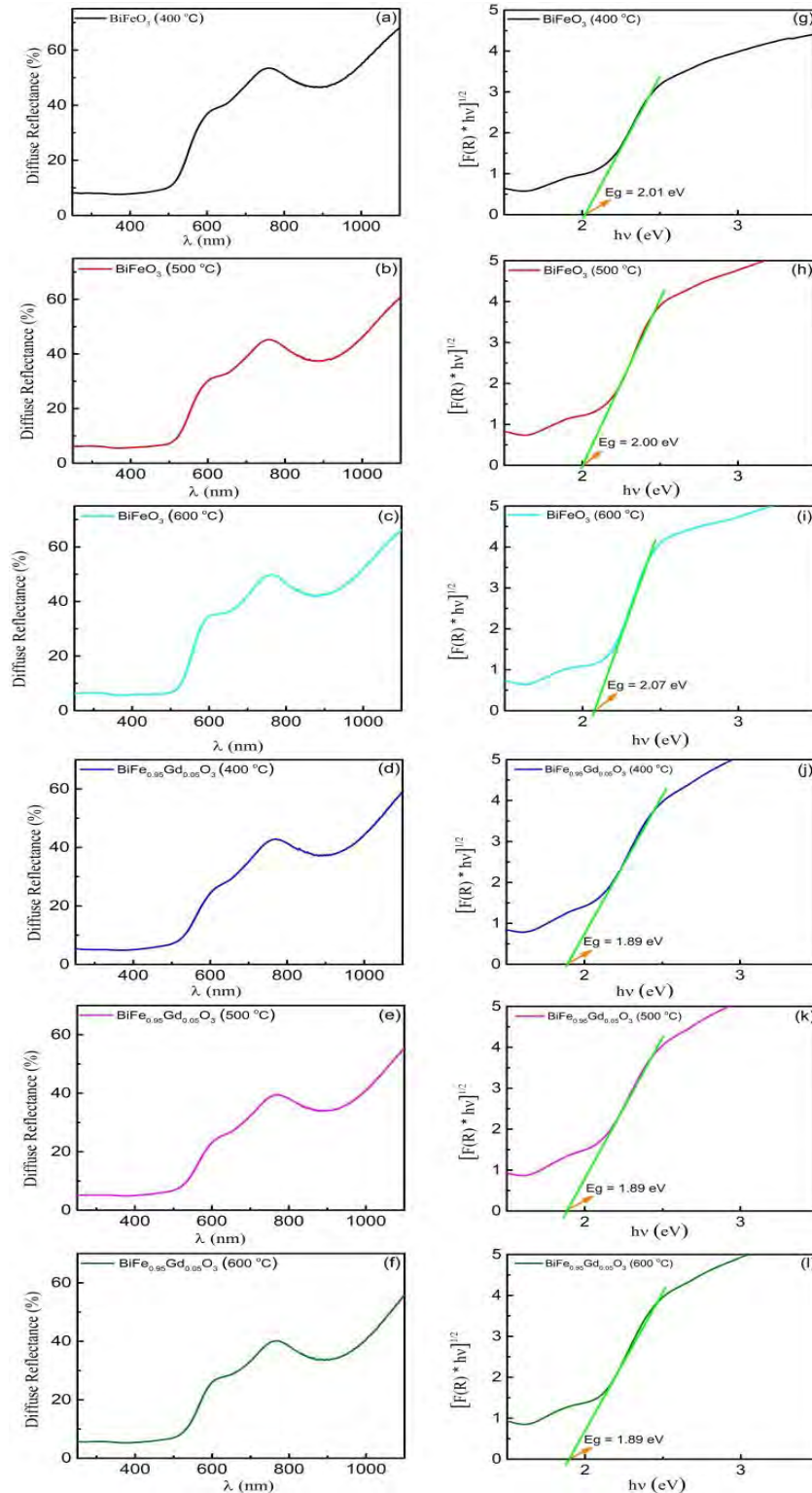
Figure 4.11: Diffuse reflectance spectra and their corresponding band gap of $BiFe_{1-x}Gd_xO_3$ (x = 0.00, 0.05) nanoparticles annealed at temperature ranging from 400 °C to 600 °C.

From the KM plot, the estimated band gap energy of the synthesized nanoparticles were inserted in table 8. The determined values are quite comparable with other reported values [36, 37].

Table:8

The table shows the band gap energy of $BiFe_{1-x}Gd_xO_3$ (x = 0.00, 0.05) nanoparticles annealed at temperature ranging from 400 °C to 600 °C.

Annealing temperature (°C)	Sample	Particle size (nm)	Band gap energy (Eg) (eV)	Sample	Particle size (nm)	Band gap energy (Eg) (eV)
400	$BiFeO_3$	57	2.01	$BiFe_{0.95}Gd_{0.05}O_3$	57	1.89
500	$BiFeO_3$	75	2.00	$BiFe_{0.95}Gd_{0.05}O_3$	46	1.89
600	$BiFeO_3$	124	2.07	$BiFe_{0.95}Gd_{0.05}O_3$	35	1.89

From table it is observed that, the band gap energy of 5% Gd doped $BiFeO_3$ nanoparticles is decreased compared to the undoped $BiFeO_3$ nanoparticles. So, it can be conclude that the band gap energy of $BiFeO_3$ nanoparticles can be controlled by doping of Gd in place of Fe in $BiFeO_3$. The smaller band gap energy (Eg) suggests that Gd-doped $BiFeO_3$ nanoparticles can be used in energy related applications e.g. for solar hydrogen production via water splitting [11].

References:

[1] Hu, W., Chen, Y., Yuan, H., Li, G., Qiao, Y., Qin, Y., Feng, S., "Structure, Magnetic, and Ferroelectric Properties of $Bi_{1-x}Gd_xFeO_3$ Nanoparticles", J. Phys. Chem. C., 115, 8869, 2011.

[2] Hasan, M., Islam, M. F., Mahbub, R., Hossain, M. S., Hakim, M. A., "A soft chemical route to the synthesis of $BiFeO_3$ nanoparticles with enhanced magnetization", Mat. Res. Bull., 73, 179, 2016.

[3] Sagdeo, A., Mondol, P., Upadhyay, A., Sinha, A. K., Srivastava, A. K., Gupta, S. M., Chowdhury, P., Ganguli, T., Deb, S. K., "Correlation of microstructural and physical properties in bulk $BiFeO_3$ prepared by rapid liquid-phase sintering", Solid State S., 18, 1, 2013.

[4] Valant, M., Axelsson, A. K., Alford, N., "Preculiarities of solid-state synthesis of multiferroic polycrystalline $BiFeO_3$", Chem. Mater., 19, 5431, 2007.

[5] Lu, J., Qiao, L. J., Fu, P.Z., Wu, Y. C., "Phase equilibrium of Bi_2O_3-Fe_2O_3 pseudo-binary system and growth of $BiFeO_3$ single crystal", J. Cryst. Grow., 318, 936, 2011.

[6] Al-Haj, M., "X-ray diffraction and magnetization studies of $BiFeO_3$ multiferroic compounds substituted by Sm^{3+}, Gd^{3+}, Ca^{2+}", Cryst. Res. Tech., 45, 89, 2010.

[7] Das, R., Sarkar, T., Mandal, K., "Multiferroic properties of Ba^{2+} and Gd^{3+} co-doped bismuth ferrite: magnetic, ferroelectric and impedance spectroscopic analysis", J. Phys. D: Appl. Phys., 45, 455002, 2012.

[8] Mukherjee, A., Basu, S., Manna, P. K., Yusuf, S. M., Pal, M., "Giant magnetodielectric and enhanced multiferroic properties of Sm doped bismuth ferrite nanoparticles", J. Phys. Chem. C., 2, 5885, 2014.

[9] Khomchenko,V. A., Kiselev, D. A., Bdikin,I. K., Shvartsman, V. V., Borisov, P., Kleemann, W., Vieira,J. M., Kholkin, A. L., "Crystal structure and multiferroic properties of Gd-substituted $BiFeO_3$", Appl. Phys. Lett., 93, 262905, 2008.

[10] Lotey, G.S., Verma, N. K., "Structural, magnetic, and electrical properties of Gd-doped $BiFeO_3$ nanoparticles with reduced particle size", J. Nanopart. Res., 14, 742, 2012.

[11] Guo, R., Fang, L., Dong, W., Zheng, F., and Shen, M., "Enhanced Photocatalytic Activity and Ferromagnetism in Gd Doped $BiFeO_3$ Nanoparticles", J. Phys. Chem. C., 114, 21390, 2010.

[12] Liu, J., Fang, L., Zheng, F., Ju, S., Shen, M. R., "Enhancement of magnetization in Eu doped $BiFeO_3$ nanoparticles", Appl. Phys. Lett., 95, 022511, 2009.

[13] Selbach, S. M., Tybell, T., Einarsrud, M. A., Grande, T., "Size-Dependent Properties of Multiferroic $BiFeO_3$ Nanoparticles", Chem. Mater., 19, 6478, 2007.

[14] Basith, M. A., Kurni, O., Alam, M. S., Sinha, B. L. and Bashir Ahmmad, "Room temperature dielectric and magnetic properties of Gd and Ti co-doped $BiFeO_3$ ceramics", J. Appl. Phys., 115, 024102, 2014.

[15] Makhdoom, A. R., Akhtar, M. J., Rafiq, M. A., Siddique, M., Iqbal, M., Hasan, M. M., "Enhancement in the multiferroic properties of $BiFeO_3$ by charge compensated aliovalent substitution of Ba and Nb", AIP Advances, 4, 037113, 2014.

[16] Cheng, Z., Wang, X., Dou, S., Kimura, H., Ozawa, K., "Improved ferroelectric properties in multiferroic $BiFeO_3$ thin films through La and Nb codoping", Phys. Rev. B., 77, 092101, 2008.

[17] Qi, X. D., Dho, J., Tomov, R., Blamire, M., Driscoll, J. L. M., "Greatly reduced leakage current and conduction mechanism in aliovalent –ion-doped $BiFeO_3$", App. Phys. Lett., 86, 062903, 2005.

[18] Ahmmad, B., Kanomata, K., Koike, K., Kubota, S., Kato, H., Hirose, F., Billah, Areef, Jalil, M. A., Basith, M. A., "Large difference between the magnetic properties of Ba and Ti co-doped $BiFeO_3$ bulk materials and their corresponding nanoparticles prepared by ultrsonication", Under review, J. Phys. D: Appl. Phys.

[19] Chang, C., Mao, D., "Thermal dehydration kinetics of a rare earth hydroxide, $Gd(OH)_3$", Int. J. Chem. K., 39, 75, 2007.

[20] Cheng, F., Zhang, N., Yang, F., Wang, S., Song, G., "Effect of Cr substitution on the structure and electrical properties of $BiFeO_3$ ceramics", J. Phys. D: Appl. Phys., 40, 7799, 2007.

[21] Wu, M. S., Huang, Z. B., Han, C. X., Yuan, S. L., Lu, C. L., Xia, S. C., "Enhanced multiferroic properties of $BiFeO_3$ ceramics by Ba and high-valence Nb co-doping", Solid State Com., 152, 2142, 2012.

[22] Jonscher, A. k., "The ,,universal" dielectric response", Nature, 267, 673, 1977.

[23] Pandit, P., Satapathy, S., and Gupta, P. K., "Effect of La substitution on conductivity and dielectric properties of $Bi_{1-x}La_xFeO_3$ ceramics: An impedance spectroscopy analysis", Physica B., 406, 2669, 2011.

[24] Maxwell, J. C., "A Treatise on Electricity and Magnetism", Clarendon Press, Oxford, 1873.

[25] Wagner, K. W., Theor, Z., "Zur Theorie der unvollkommenen Dielektrika", Ann. Phys., 40, 817, 1913.

[26] Yang, C., Jiang, J. S., Qian ,F. Z., Jiang, D. M., Wang, C. M., Zhang, W. G., "Effect of Ba doping on magnetic and dielectric properties of nanocrystalline $BiFeO_3$ at room temperature", J. Alloys Compd., 507, 29, 2010.

[27] Makhdoom, A. R., Akhtar, M. J., Rafiq, M. A., and Hassan, M. M., "Investigation of transport behavior in Ba doped $BiFeO_3$", Ceram. Int., 38, 3829, 2012.

[28] Choudhury, B.,Choudhury, A., "Room temperature ferromagnetism in defective TiO_2 nanoparticles: Role of surface and grain boundary oxygen vacancies", J. App. Phys., 114, 203906, 2013.

[29] Kumar, D., Banerjee, A., "Coexistence of interacting ferromagnetic clusters and small antiferromagnetic clusters in $La_{0.5}Ba_{0.5}CoO_3$", J. Phys.: Condens Matter., 25, 216005, 2013.

[30] Park, T. J., Papaefthymiou, G. C., Viescas, A. J., Moodenbaugh, A. R., Wong, S. S., "Size-dependent magnetic properties of single-crystalline multiferroic $BiFeO_3$ nanoparticles", Nano Letters., 7, 766, 2007.

[31] Pradhan, S. K., Roul, B. K., "Effect of Gd doping on structural, electrical and magnetic properties of $BiFeO_3$ electroceramic", J. Phy. Chem. S., 72, 1180, 2011.

[32] Pradhan, S. K., Das, J., Rout, P. P., Das, S. K., Mishra, D. K., Sahu, D. R., Pradhan, A. K., "Defect driven multiferroicity in Gd doped $BiFeO_3$ at room temperature", J. Magn. Magn. Mater., 322, 3614, 2010.

[33] Ahmmad, B., Islam, M. Z., Billah, A., Basith, M. A., "Anomalous coercivity enhancement with temperature and tunable exchange bias in Gd and Ti co-doped $BiFeO_3$ multiferroics", J. Phys. D: Appl. Phys., 49, 095001, 2016.

[34] Hasan, M., Hakim, M. A., Basith, M. A., Hossain, M. S., Ahmmad, B., Zubair, M. A., Hussain, A.,and Islam, M. F., "Size dependent magnetic and electrical properties of Ba-doped nanocrystalline $BiFeO_3$", AIP Advances, 6, 035314, 2016.

[35] Pavana, S. V. M., Karthik, C., Ubic, R., Rao, M. S. R., and Sudakar, C., "Tunable bandgap in $BiFeO_3$ nanoparticles: The role of microstrain and oxygen defects", Appl. Phys. Lett., 103, 022910, 2013.

[36] Joshi, U. A., Jang, J. S., Borse, P. H., Lee, J. S., "Microwave synthesis of single-crystalline perovskite $BiFeO_3$ nanocubes for photoelectrode and photocatalytic applications", Appl. Phys. Lett., 92, 242106, 2008.

[37] Gao, F., Chen, X., Yin, K., Dong, S., Ren, Z., Yuan, F., Yu, T., Zou, Z., Liu, J. M., "Visible-Light Photocatalytic Properties of Weak Magnetic $BiFeO_3$ Nanoparticles", Adv. Mater., 19, 2889, 2007.

Chapter 5

Summary and Conclusions

5.1 Summary and Conclusions

➢ The nominal compositions of $BiFe_{1-x}Gd_xO_3$ (x = 0.00, 0.05) nanoparticles were produced successfully using sol-gel method.

➢ The Gd substitution in place of Fe in $BiFeO_3$ nanoparticles significantly reduced the particle size up to ~35 nm.

➢ The leaky behavior of the synthesized nanoparticles was also suppressed due to Gd substitution and increasing annealing temperature. The suppression of leakage current density improved the ferroelectric behavior of the synthesized nanoparticles.

➢ The substitution of Gd was found to be helpful to stabilize the dielectric constant over a wide range of high frequencies by suppressing dispersion at low frequencies.

➢ For Gd-doped $BiFeO_3$ nanoparticles the room temperature magnetic parameters such as saturation magnetization (M_s) and remanent magnetization (M_r) decreased gradually with increasing annealing temperature, but the values are many folds higher than their bulk counterparts.

➢ The estimated band gap energy of the synthesized nanoparticles indicates that the substitution of Gd can reduce band gap energy of multiferroic $BiFeO_3$ nanoparticles.

➢ The low band gap of the synthesized nanoparticles might have potentiality in the visible light driven photocatalytic applications such as solar hydrogen production via water splitting.

Finally we may conclude that 5 % Gd doped BiFeO$_3$ nanoparticles annealed at 600 °C may be a promising multiferroic and efficient photocatalyst.

5.2 Suggestion for future work

10% Gd doped BiFeO$_3$ nanoparticles will be synthesized and their structural, electrical, dielectric, magnetic and optical properties will be investigated. Moreover in the present investigation, the structural, electric, dielectric, magnetic and optical properties of the synthesized nanoparticles were investigated and we observed improved electric, dielectric and magnetic properties of Gd-doped BiFeO$_3$ nanoparticles compared to the undoped BiFeO$_3$ nanoparticles. It might be interesting to investigate further the temperature dependent dielectric and magnetic properties of all the samples which will be helpful for finding suitable application of these materials.

From the electric measurements, a significant reduction in the leakage current densities was observed in the fabricated nanoparticles which may be caused due to the reduction of oxygen vacancies. Hence to confirm the existence of oxygen vacancies and oxidation states of the elements in each composition XPS measurements will be performed. The O 1s spectra of the samples will be analyzed to estimate the concentration of oxygen vacancies in the undoped and Gd-doped BiFeO$_3$ nanoparticles. Finally by using the synthesized nanoparticles thin film may be deposited on glass substrate using spin coater and may be carried out their characteristics.